

# POLITECNICO DI MILANO

Scuola di Ingegneria Industriale e dell'Informazione

Corso di Laurea Magistrale in  
Ingegneria dell'Automazione



Design of an Automatic Method for the Soft-sensing of the Surfactant Concentration  
in a Mini-plant of Hydroformylation of Long-chain Alkenes in Microemulsions

Relatore: Prof. Marcello Farina

Correlatore: MSc. Markus Illner

Tesi di Laurea di:

Angela ALZATE

Matr. 852434

Anno Accademico 2017 - 2018



# Sommario

L'innovativo processo dell'idroformilazione di alcheni a catena lunga in microemulsioni è considerato una soluzione sostenibile per la produzione di aldeidi da prodotti biologici derivati. L'idea è stata sviluppata in un mini-impianto costruito all'Technische Universität Berlin. Tuttavia, il recupero del costoso catalizzatore utilizzato nel sistema pone ancora delle sfide importanti. Il processo di separazione di fase usato per questo obiettivo è infatti altamente dipendente dalla concentrazione di tensioattivo, il cui livello non è misurabile. Per risolvere questo problema in questa tesi, sono proposte metodologie per la modellistica sperimentale per descrivere il comportamento della separazione di fase della microemulsione e per il processamento di immagini per la rilevazione automatica del livello delle fasi. Questi metodi sono qui applicati e integrati per lo sviluppo di un *soft-sensor* per la stima della concentrazione di tensioattivo. Tutto questo ha un ruolo fondamentale nell'ottimizzazione del processo e per garantire un funzionamento stabile della separazione di fase nel *decanter*.

**Keywords:** Modellistica sperimentale, Rilevazione di livello, Soft-sensor, Microemulsione, Separazione di fase, Idroformilazione.



# Abstract

A novel process concept for the hydroformylation of long-chain alkenes in microemulsion is investigated as a environmental-friendly and sustainable solution for the production of aldehydes from biobased products. A proof of concept has been devised in a hydroformylation mini-plant at TU Berlin. However, challenges in the efficient recycle of the expensive catalyst used in the reaction still remain. The phase separation process used for this purpose highly depends on the surfactant concentration of the mixture, which is not possible to track. Hence, black-box modelling methodologies to describe the phase separation behavior and image processing operations for phase level detection are applied and integrated into the development of a soft-sensor for the surfactant concentration. The latter serve as part of the solution for the full dynamic real time optimization framework, and to obtain a stable three-phase separation operation inside the settler.

**Keywords:** Black-Box Modelling, Microemulsion, Phase separation, Level detection, Soft-sensor.



# Contents

<b>1</b>	<b>Introduction</b>	<b>1</b>
1.1	Motivation of this work . . . . .	1
1.2	Objectives of the thesis . . . . .	2
1.3	Outline . . . . .	4
<b>2</b>	<b>Description of the Process Under Study</b>	<b>5</b>
2.1	Phase Separation in Microemulsions . . . . .	6
2.2	The mini-plant at TU Berlin: General overview . . . . .	7
2.2.1	Piping and Instrumentation Diagram . . . . .	7
2.2.2	Relevant Equipment and Instrumentation . . . . .	8
2.2.3	Materials . . . . .	9
2.2.4	Process conditions . . . . .	10
2.3	Role of the phase separation model in the optimization framework . . . . .	11
2.3.1	Settler model . . . . .	13
2.4	Overview of the proposed solution . . . . .	14
<b>3</b>	<b>Image Processing Algorithm for Phase Level detection</b>	<b>17</b>
3.1	Image processing . . . . .	17
3.1.1	Color spaces . . . . .	17
3.1.2	Image Filtering . . . . .	18
3.1.3	Edge detection . . . . .	19
3.2	Phase level detection: main steps . . . . .	20
3.3	Color detection . . . . .	22
3.4	Boundary detection . . . . .	22
3.5	Conversion from level to volumetric fraction . . . . .	24
3.6	Cases of success and failure . . . . .	25
<b>4</b>	<b>Experimental design and black-box modelling of the phase separation process</b>	<b>29</b>
4.1	General Methodology for Identification . . . . .	29
4.2	Experimental Design . . . . .	30
4.2.1	The a-priori knowledge of the system and variables of interest . . . . .	30
4.2.2	Experimental setting . . . . .	32
4.3	Experimental observations . . . . .	34
4.3.1	Sources of error . . . . .	34
4.4	Collection of Data . . . . .	35
4.4.1	Volume corrections . . . . .	36

---

4.5	Preliminary analysis . . . . .	37
4.5.1	Relative phase level vs. temperature . . . . .	38
4.5.2	Temperature boundaries vs. components concentration . . . . .	41
4.6	Model family selection . . . . .	42
4.7	Parameter estimation . . . . .	43
4.7.1	Polynomial regression . . . . .	44
4.8	Model Validation . . . . .	45
4.8.1	Basic concept . . . . .	45
4.8.2	Selection of the suitable model for phase separation . . . . .	46
<b>5</b>	<b>Integration in the Control System Siemens PCS7</b>	<b>55</b>
5.1	Operating Region plot . . . . .	55
5.2	Soft-sensor for surfactant concentration and oil to water ratio . . . . .	56
5.3	Communication architecture . . . . .	57
5.4	Visualization in Siemens PCS7 . . . . .	58
<b>6</b>	<b>Conclusions and Outlook</b>	<b>61</b>
<b>A</b>	<b>Density functions of the components</b>	<b>63</b>
	<b>Bibliography</b>	<b>65</b>



# List of Figures

2.1	Main reaction carried out at TU Berlin mini-plant . . . . .	5
2.2	Representation of the phase separation behavior of a microemulsion. Images taken from <a href="#">Illner, Müller, et al., 2016a</a> which is an extension of <a href="#">Stubenrauch, 2008</a> work . . . . .	6
2.3	Simplified P&ID of the mini-plant at TU Berlin. Taken from <a href="#">Illner, Müller, et al., 2016a</a> . . . . .	8
2.4	Photo of the mini-plant. Taken from <a href="#">Illner, Müller, et al., 2016a</a> . . . . .	9
2.5	Settler unit installed in the mini-plant . . . . .	9
2.6	Control strategy at TU Berlin hydroformylation mini-plant . . . . .	12
2.7	Scheme of the dynamic model of the mini-plant . . . . .	12
2.8	Scheme of the separator unit model . . . . .	13
2.9	Switches for . . . . .	14
2.10	Overview of the general solution . . . . .	15
3.1	The hue-saturation representation. Image taken from <a href="#">Moeslund, 2012</a> . . . . .	18
3.2	The HSV color space representation. Image taken from <a href="#">Bora et al., 2015</a> . . . . .	18
3.3	Flow diagram of image processing script for phase level detection . . . . .	21
3.4	Original image cropped to Region of Interest . . . . .	21
3.5	Threshold definition for all phases . . . . .	26
3.6	Example of water level recognition using canny edge detection . . . . .	27
3.7	Successful and failure cases in the level detection algorithm . . . . .	27
4.1	Flow Chart of system identification methodology. Redrawn from <a href="#">Soderstrom and Stoica, 1989</a> . . . . .	30
4.2	Three phase separation of the mixture at different temperatures and a constant concentration of surfactant $\gamma = \gamma_0$ . . . . .	32
4.3	Schematic and real set-up of the experiments. 1. Thermostat, 2. Jacketed vessel, 3. Magnetic stirrer, 4. Thermometer with Pt100, 5. Camera and tripod . . . . .	33
4.4	Phase separation evolution for variable temperatures and concentrations $\alpha = 0.5$ , $\gamma = 0.075$ , $X = 0$ . . . . .	34
4.5	Phase separation evolution for variable temperatures and concentrations $\alpha = 0.5$ , $\gamma = 0.07$ , $X = 0.2$ . . . . .	35
4.6	Discarded experiment with concentrations $\alpha = 0.4$ , $\gamma = 0.085$ , $X = 0.4$ and $T = 69^\circ\text{C}$ . . . . .	35

4.7	Determination of the relative level of the phases: $h_{oil_{pix}}$ , $h_{surf_{pix}}$ , $h_{wat_{pix}}$ in terms of pixels. . . . .	36
4.8	Phase separation state for different temperatures at concentrations $\alpha = 0.5$ , $\gamma = 0.080$ and $X = 0$ . . . . .	38
4.9	Experimental and model comparisson for the relative level oil phase as a function of temperature. Concentrations $\alpha = 0.5$ , $\gamma = 0.080$ and $X = 0$ . . . . .	39
4.10	Polynomial fitting or order two for the three phase data at concentrations $\alpha = 0.5$ , $\gamma = 0.080$ and $X = 0$ . . . . .	40
4.11	Fitted curve of oil phase using sigmoidal trigger functions with different slopes: $a = 5$ , $a = 10$ and $a = 50$ . Concentrations $\alpha = 0.5$ , $\gamma = 0.080$ and $X = 0$ . . . . .	40
4.12	Fitted curve of water phase using sigmoidal trigger functions with different slopes: $a = 5$ , $a = 10$ and $a = 50$ . Concentrations $\alpha = 0.5$ , $\gamma = 0.080$ and $X = 0$ . . . . .	41
4.13	Temperature boundaries vs. Surfactant concentration for $\bar{\alpha} = 0.5$ and $\bar{X} = 0$ . Experimental data and fitted curve. . . . .	42
4.14	Temperature boundaries vs. Surfactant concentration for $\bar{\alpha} = 0.5$ and $\bar{X} = 0.4$ . Experimental data and fitted curve. . . . .	43
4.15	General model for the three phase separation state . . . . .	43
4.16	Schematic of LOOCV partitions. Image taken from <a href="#">James et al., 2014</a> . . . . .	46
4.17	Comparisson of MSE and $R^2$ values for different model structures of the lower temperature boundary . . . . .	48
4.18	Comparison of MSE and $R^2$ values for different model structures of the upper temperature boundary . . . . .	48
4.19	Temperature boundaries fitted surfaces for the experimental data. Constant concentration $\alpha = 0.5$ and variable concentrations $\gamma$ and $X$ . . . . .	49
4.20	Comparisson of MSE and $R^2$ values for different model structures of the relative level of oil phase . . . . .	51
4.21	Fitted surface for relative level of oil phase at constant concentration $\alpha = 0.5$ and $X = 0$ and variable concentrations $\gamma$ and $T$ . . . . .	51
4.22	Comparisson of MSE and $R^2$ values for different model structures of the relative level of water phase . . . . .	52
4.23	Fitted surface for relative level of water phase at constant concentration $\alpha = 0.5$ and $X = 0$ and variable concentrations $\gamma$ and $T$ . . . . .	52
4.24	Fitted surface for relative level of oil phase at constant concentration $\alpha = 0.5$ and $X = 0$ and variable concentrations $\gamma$ and $T$ . . . . .	53
4.25	Fitted surface for relative level of water phase at constant concentration $\alpha = 0.5$ and $X = 0$ and variable concentrations $\gamma$ and $T$ . . . . .	53
5.1	Operating region for a measured temperature of $T = 78.2^\circ\text{C}$ and conversion $X = 0$ . . . . .	56
5.2	Block diagram for determination of the operating region plot at actual process conditions . . . . .	56
5.3	Soft-Sensor structure, inputs and outputs . . . . .	57
5.4	Operating region plot with estimated values of $\alpha$ and $\gamma$ (blue dot) and set-point (red rectangle) . . . . .	58

---

5.5	Scheme of communication for the automatic solution . . . . .	58
5.6	Soft-sensor and processed image integrated to the Control system PCS7 . . . . .	60



# List of Tables

2.1	Features of phase separation regimes . . . . .	11
2.2	Minimum and maximum concentration of liquid components . . . . .	11
3.1	Example of steps in level detection algorithm . . . . .	23
A.1	Minimum and maximum concentration of liquid components . . . . .	63



# Abbreviations

<b>RCH/RP</b>	Ruhrchemie/Rhône-Poulenc process for catalyst recovery
<b>TU Berlin</b>	Technische Universität Berlin
<b>P&amp;ID</b>	Piping and Instrumentation Diagram
<b>GC</b>	Gas Chromatography Analysis or Gas Chromatograph
<b>CAS</b>	Chemical Abstracts Service
<b>D-RTO</b>	Dynamic Real Time Optimization
<b>NLP</b>	Nonlinear Programming
<b>MINLP</b>	Mixed Integer Nonlinear Programming
<b>RGB</b>	Red, Green, Blue color space
<b>HSV</b>	Hue, Saturation, Value color space
<b>ROI</b>	Region of Interest
<b>LS</b>	Least Squares technique for parameter estimation
$R^2$	Coefficient of determination
<b>MSE</b>	Mean Squared Error
<b>SSE</b>	Sum of the Squares of residuals
<b>SST</b>	Total sum of squares
<b>LOOCV</b>	Leave One-Out Cross Validation technique
<b>HMI</b>	Human Machine Interface
<b>SCADA</b>	Supervisory Control And Data Acquisition System
<b>OPC</b>	Object Linking and Embedding for Process Control





# Nomenclature

## Symbols

$\alpha$	Oil to water ratio	[g/g]
$\gamma$	Surfactant concentration	[g/g]
$\varphi$	Relative level phase, Volume fraction	[%]
$\rho$	Density	[g/mm <sup>3</sup> ]
$\sigma$	Standar deviation	
$A$	Area, gray-level information	
$a$	Steepness of sigmoid function	
$f$	Function	
$G$	Gaussian function or Gradient	
$h$	height, level	
$m$	Mass of component	[g]
$R$	Length	[mm]
$R$	Radius	[mm]
$T$	Temperature	[°C]
$W_p$	Normalization factor	
$X$	Conversion	[g/g]
$y$	Vertical direction, dependent variable	
$cat$	Catalyst	
$corr$	Corrected	
$dod$	1-dodecene	
$foam$	Surfactant rich layer known as foam	

<i>G</i>	Global
<i>h</i>	Upper boundary
<i>L</i>	Local
<i>l</i>	Low boundary
<i>mag</i>	Magnet of the stirrer
<i>mid</i>	Middle phase or surfactant rich phase
<i>mix</i>	Mixture, Surfactant rich phase
<i>oil</i>	Oily components: 1-dodecene, 1-tridecanal
<i>sp</i>	Setpoint
<i>surf</i>	Surfactant, Surfactant rich phase
<i>surf</i>	Surfactant
<i>tdc</i>	Tridecanal
<i>tot</i>	Total
<i>wat</i>	Water phase
<i>x</i>	Horizontal axis
<i>y</i>	Vertical axis

# Chapter 1

## Introduction

### 1.1 Motivation of this work

Everyday, more and more companies of the chemical industry are putting their efforts into developing new methods to reduce the harm caused to the environment, to preserve the natural resources and, as described in the twelve principles of green chemistry by [Anastas and Eghbali, 2010](#), to prevent waste. A novel sustainable solution for the production of aldehydes by using biobased products as feedstocks is actually being investigated. Aldehydes are relevant in the industry worldwide because they can be easily converted into alcohols, which are used as solvents, detergents or plastifiers. They are also used in pharmaceuticals, dyes and in the production of flavour agents and fragrances ([Jürgen et al., 2008](#)).

Aldehydes can be produced through the hydroformylation, also known as oxo synthesis. Hydroformylation is a process in which aldehydes (linear or branched) are obtained due to the reaction of alkenes and Syngas (mixture of CO and H<sub>2</sub>) in the presence of a catalyst ([Roelen, 1944](#)). In the past few decades different types of oxo processes have been developed. Initially, a Cobalt-based catalyst was used in hydroformylation processes (e.g. by BASF, Ruhrchemie, Kuhlmann) but, because of its lower activity, the reaction conditions were severe with pressure ranges of 200-350 bar and temperatures of 150-180 °C ([Ünveren, 2004](#)). Later, a rhodium-based catalyst modified with phosphines was used enabling lower pressures due to higher activity (18-60 bar) and medium temperatures (85 - 130 °C). Using rhodium as a catalyst metal instead of cobalt not only led to milder reaction conditions but also high in terms of chemo-selectivity and high yield. Nonetheless, the price of rhodium compared to cobalt is very high, therefore it is of great importance to recover it efficiently.

The Ruhrchemie/Rhône-Poulenc (RCH/RP) process, developed in the 1980s, offers a technique for catalyst recovery by solubilizing the ligand-modified rhodium-based catalyst in an aqueous phase. This leads to separation by simple decantation ([Kohlpaintner et al., 2001](#)). The advantages of this process include the mild operating conditions (pressure: up to 60 bar, temperature: up to 120 °C) and the negligible amount of catalyst lost through the product stream ([Haumann et al.,](#)

2002). However, the application of this method is limited only to short-chain alkenes due to their higher solubility in aqueous phase and high reaction rates. Consequently, major difficulties is found in the use of long-chain olefines (e.g. biobased products), for the production of aldehydes.

The Collaborative Research Center Transregio 63 "Integrated Chemical Processes in Liquid Multiphase Systems" (InPROMPT) is investigating the hydroformylation of long-chain alkenes. The key to enhance the miscibility between the alkene and catalyst is the addition of a surfactant to the compounds, forming a microemulsion and permitting the subsequent separation of the expensive catalyst.

In order to investigate the hydroformylation of long-chain alkenes in microemulsions, a mini-plant has been constructed at Technische Universität Berlin. The mini-plant is based on a mixer-settler concept in which, after the reaction has taken place, the mixture is separated inside the settler into 3 phases: An oil rich phase (containing mainly the aldehyde), a surfactant rich phase and a catalyst rich phase (water phase). Proof of concept for continuous operation with high selectivity and yield was achieved. (Illner, Pogrzeba, et al., 2016b).

The operating region for the separation of the microemulsion depends on its temperature and on the concentration of the compounds. In particular, the separation state of the mixture is highly sensitive to the surfactant concentration. Long-term operations carried out on the system showed that, due to the recycle operation with three independent recycle streams, shifts and accumulations in the surfactant concentrations could occur. Together with the ongoing reaction and product formation, this results in the loss of the desired three phase separation state (Illner, Pogrzeba, et al., 2016b). While the reacting compounds and the overall oil-to-water ratio can be analyzed via liquid gas chromatography, the surfactant concentration is not promptly accessible with reasonable sampling times. Therefore, the application of advanced process control methods is strived for to enable the safe, stable, and efficient operation of such process. In particular, the development of a soft-sensor for the surfactant concentration in the system is mandatory to increase the observability of the process and enable further optimization of plant trajectories.

To develop a soft-sensor for the surfactant concentration, it is necessary to detect the actual state of the phase separation, which has been done manually so far. To ensure a full automatic operation, a web camera captures the actual state of the phase separation and an image processing algorithm must be developed to detect the level of the phases automatically.

## 1.2 Objectives of the thesis

The main scope of this thesis is to design an automatic procedure that quantifies the surfactant concentration based on the state of the phase separation of the microemulsion, which is necessary for a stable operation of the mini-plant. This includes also the development of a suitable image processing algorithm to analyze

the actual state of the phase separation automatically.

More specifically, the objective of the thesis is threefold:

1. To perform the necessary experiments for the collection of the data, to analyze them, and to use such data for the development of a black-box model that best represents the behavior of the phase separation in microemulsions.
2. To develop of an automated image processing algorithm that evaluates the state of the phase separation.
3. To consolidate the image processing algorithm with the obtained model to create a soft-sensor for the surfactant concentration and the oil-to-water ratio. Finally, the soft-sensor is integrated in the Siemens PCS7 control system.

## 1.3 Outline

The remainder of the thesis consists of the following chapters:

**In Chapter 2** a description of the hydroformylation of long-chain alkenes in microemulsions process is given. In particular, the mini-plant at TU Berlin is described in detail. Also, the basic theory behind the phase separation of amicroemulsion in the context of previous studies is discussed in detail.

**Chapter 3** presents the solution given for the automatic level detection through image processing algorithms. Mainly, the color segmentation and contour detection methods are explained.

**In Chapter 4** the necessary procedure for the black-box modelling is described: the experimental setting, the selection of the appropriate model, the estimation of parameters and the validation of the model.

**In Chapter 5** the integration of the image processing algorithm with the experimental model for the construction of a soft-sensor for the oil-to-water ratio and surfactant concentration is described. Also, its integration into the control system Siemens PCS7 and the design of the visualization panel is shown. The latter allows the operator to observe the prediction of the actual state of separation inside the settler unit.

**In Chapter 6** a summary of the work and the conclusions are given. Here, the future work and possible improvements are also discussed.

## Chapter 2

# Description of the Process Under Study

As shortly discussed in the Introduction, the main reaction in the hydroformylation process involves the alkene 1-dodecene, Syngas (mixture of CO and H<sub>2</sub>), a rhodium-based catalyst solution and surfactant Marlipal 24/70 (see Figure 2.1). Due to the high cost of this catalyst complex, a phase separation process is necessary for its efficient recovery. The phase separation of the microemulsion formed at the reactor depends on the temperature and the concentration of the compounds, and more specifically to the surfactant concentration. Unfortunately, as mentioned in the Introduction, surfactant concentration cannot be measured. Therefore, understanding and describing the phase separation behavior of this microemulsion is necessary for the construction of a suitable model, that can be used for the soft-sensing of the surfactant concentration and eventually a stable and cost-efficient operation of the mini-plant.

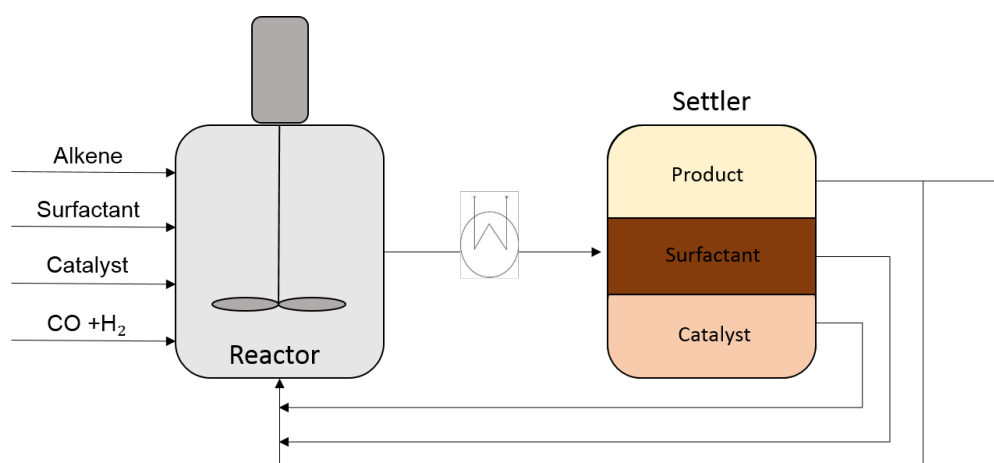


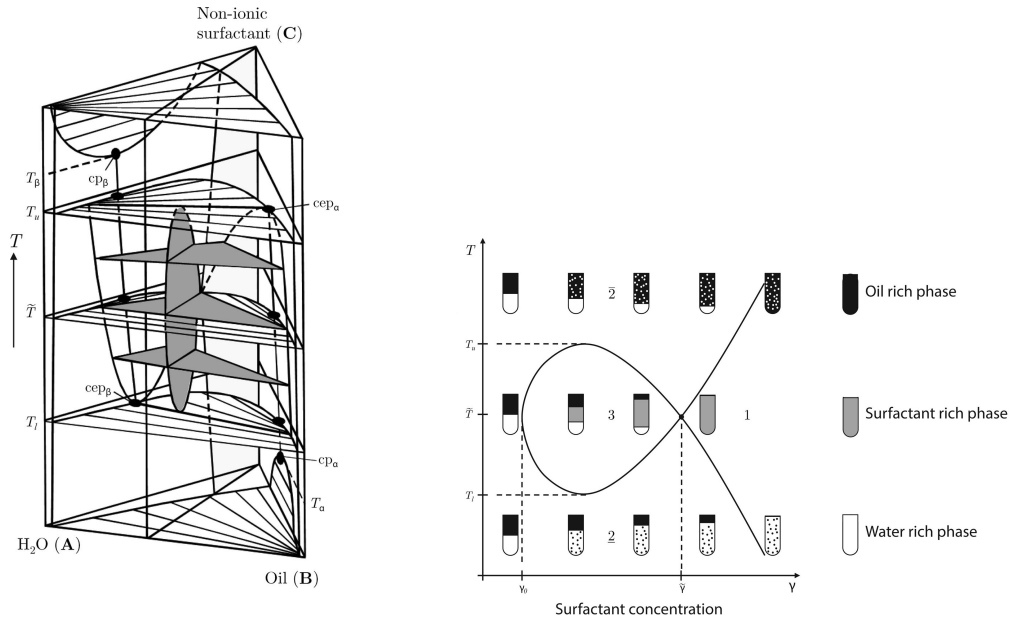
**Figure 2.1:** Main reaction carried out at TU Berlin mini-plant

In this Chapter, the theory behind the phase separation in microemulsions behavior, which is used for the further development of the model, is described in Section 2.1. Additionally, a detailed description of the mini-plant is presented in Section 2.2 to evaluate the role of the model in the optimization of the process.

## 2.1 Phase Separation in Microemulsions

A microemulsion is a mixture of water, oil, and a surfactant. The surfactant molecules may form a monolayer at the interface between the oil and water, which leads to the formation of different structures like micelles and lamellar phases (Madhav and Gupta, 2011).

Different types of phase equilibria can be found in microemulsions. They can vary depending on the concentrations of the components, temperature and pressure. Since the influence of pressure is weak compared to the effect of temperature, it is considered as constant at atmospheric pressure. The phase behavior of the oil-water-surfactant mixture can be described by Kahlweit's fish diagram 2.2b. This diagram is a cross-section of the Gibb's phase prism shown in figure 2.2a.



(a) Gibbs' phase prism. The base is a ternary plot with  $A$ : Water,  $B$ : Oil,  $C$ : Surfactant concentrations and the temperature is the ordinate of the prism.

(b) Kahlweit's fish diagram.

**Figure 2.2:** Representation of the phase separation behavior of a microemulsion. Images taken from Illner, Müller, et al., 2016a which is an extension of Stubenrauch, 2008 work

The *oil-to-water ratio*  $\alpha$  is defined as the mass fraction of the oil in the mixture of oil and water and,  $\gamma$  is specified as the *surfactant concentration* in the mixture of all three components. These are computed according to the following equations:

$$\alpha = \frac{m_{oil}}{m_{wat} + m_{oil}} \quad (2.1)$$

$$\gamma = \frac{m_{surf}}{m_{wat} + m_{oil} + m_{surf}} \quad (2.2)$$



where  $m_{oil}$ ,  $m_{wat}$ , and  $m_{surf}$  are the masses of the oil, water and surfactant respectively.

The fish diagram relates the temperature changes to variable surfactant concentration at a constant 1:1 oil-to-water ratio (Kahlweit et al., 1988). Consequently, different states of separation can be found at different temperatures and surfactant concentrations. Four types of phase equilibria can be seen in the diagram:

- Two-lower phase regime ( $\underline{2}$ ): In this regime, pure oil phase and emulsions are present.
- Three-phase region ( $\underline{3}$ ): Working at temperatures ( $T_l - T_u$ ) and concentrations ( $\gamma_0 - \gamma$ ), i.e. inside the fish body, oil (top phase) and water (bottom phase) are excess phases. The emulsion in the middle is composed with most of the surfactant.
- Single phase ( $\underline{1}$ ): No separation. Mixture is homogeneous.
- Two-upper phase regime ( $\bar{2}$ ): In this regime, an emulsion phase is located in the top and excess water phase is located at the bottom.

## 2.2 The mini-plant at TU Berlin: General overview

### 2.2.1 Piping and Instrumentation Diagram

Figure 2.3 shows the simplified P&ID diagram of the hydroformylation mini-plant, constructed at the Process Dynamics and Operations Group at Technische Universität Berlin. Also, Figure 2.4 shows the 3D model and constructed mini-plant. The plant structure is divided into three sections.

The *feed section* is composed of the feed tanks (units 1, 2, 3 marked in Figure 2.3), all designed to contain a volume of 10 L. The pumps for the 1-dodecene, catalyst solution and surfactant, feed the liquid components at 840 g/h, 400 g/h, and 200 g/h, respectively. This section holds also the gas containers (5a, 5b, 5c) for synthesis gas, pure hydrogen, and pure carbon monoxide, which are used to enable the reaction. All these elements are led into the *mixer-settler section*.

The mixer-settler section consists of a stainless-steel reactor with heating jacket (unit 6) and a decanter (unit 9). The liquid components enter the stirred tank reactor with internal total volume of 1.5 L and 0.8 L of liquid volume. The mixture is stirred with a gassing stirrer featuring a Rushton turbine with a maximum speed of 2880 rpm. The drain is positioned at 70 % height to guarantee a constant liquid level and baffles are installed within the reactor to avoid vortex formation. Subsequently, the mixture enters the phase separation unit in which, under suitable control, three main phases can be obtained: an oil-rich phase, a surfactant-rich phase and a water rich phase (see Section 2.1). The settler is equipped with a knitted mesh to enhance the phase separation and two gauge glasses for optical observation of the separation state. A detailed description of the settler construction can be found in Müller, Esche, Pogrzeba, et al., 2015. All the phases can be recycled

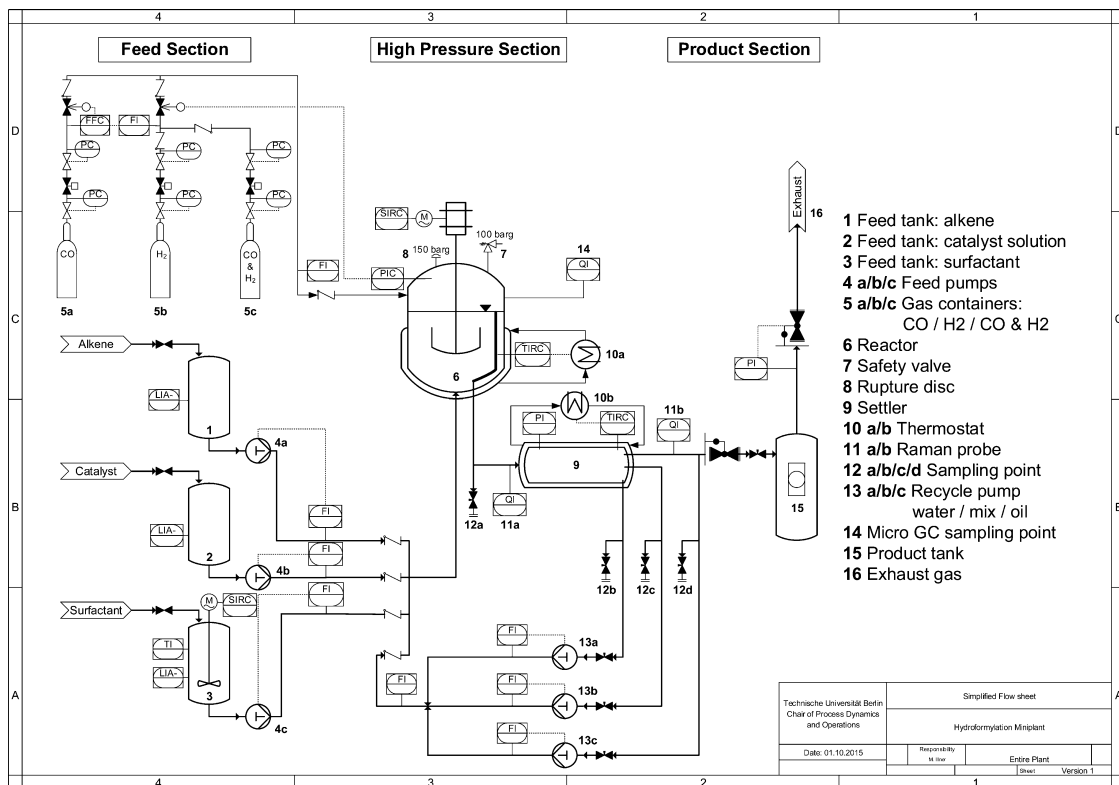


**Figure 2.3:** Simplified P&ID of the mini-plant at TU Berlin. Taken from Illner, Müller, et al., 2016a

individually back to the reactor using pumps 13a, 13b and 13c, with maximum flowrates of 1000 g/h.

Lastly, the *product storage section* includes a product container (unit 15) for the oil product and a de-pressurization unit for the removal of the synthesis gas (Illner, Müller, et al., 2016a).

## 2.2.2 Relevant Equipment and Instrumentation

The mini-plant incorporates over 50 sensors. Every second, temperature and pressure data of the tanks and streams, level information for all containers (except for the decanter) and flow measurements of all streams are available. For the analysis of the components, a micro gas chromatograph samples the gas-phase composition every 3 minutes. Using gas chromatography, liquid samples from various positions could be analyzed with respect to the oily components (1-/iso-dodecene, dodecane and 1-/iso-tridecanal). Additionally, an online-Raman spectrometer (11b in the P&ID diagram) is applied to track the reaction progress online. Oil and water phase compositions are evaluated every 2-4 hours (Müller, Illner, et al., 2017).

Along the length of the settler, temperature measurements are obtained with several Pt100 devices installed. The desired temperature can be controlled and observed. Two sight glasses allow the visual inspection of the phase separation state (see Figure 2.5).

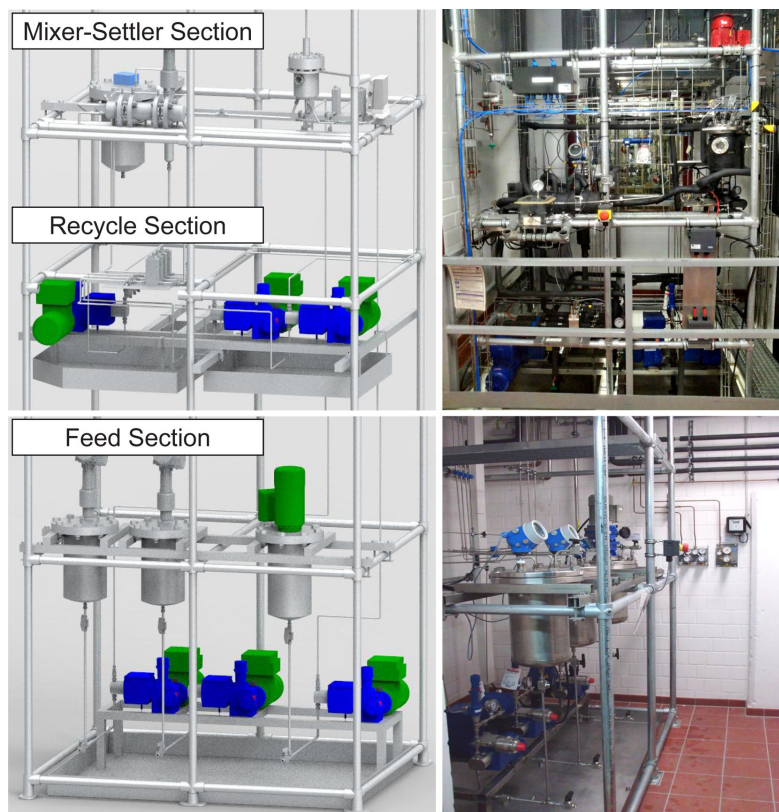


Figure 2.4: Photo of the mini-plant. Taken from Illner, Müller, et al., 2016a

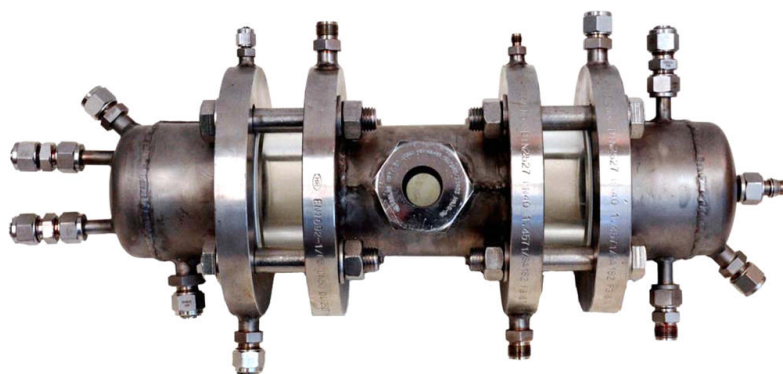


Figure 2.5: Settler unit installed in the mini-plant

### 2.2.3 Materials

The substances used in the process can be divided into 4 groups: reactants, catalyst compounds, solubilizing substances and products.

#### Reactants

The first reactant is 1-dodecene, a  $C_{12}$  alkene, which is used as an exemplary unsaturated, long-chain hydrocarbon. It is purchased from VWR (CAS Registry Number 112-41-4). The second reactant is synthesis gas with a composition of 1:1 mol %  $CO : H_2$  with a purity of 5.0, purchased from Linde.

### Catalyst compounds

The applied catalyst complex consists of a rhodium-based precursor  $[\text{Rh}(\text{acac})(\text{CO})_2]$  (CAS Registry Number 14874-82-9), sponsored by Umicore N.V., and the water-soluble ligand SulfoXantPhos (sulfonated form of XantPhos, CAS Registry Number 161265-03-8), purchased from MOLISA GmbH. Both precursor and ligand are dissolved in water.

### Solubilizing substances

The nonionic surfactant Marlipal 24/70 (CAS Registry Number 68439-50-9), sponsored by Sasol Germany GmbH, is used to enable the miscibility of 1-dodecene and the catalyst solution. Additionally, small amounts (1 wt. %) of  $\text{Na}_2\text{SO}_4$ , purchased from Th. Geyer, is added to enhance the separation of the microemulsion.

### Products

Only for experimental purposes, 1-tridecanal (CAS: 14874-82-9), which is the main product obtained from the hydroformylation reaction, is purchased from VWR with a quality of 96 %.

## 2.2.4 Process conditions

The current process conditions of the process have been defined according to previous lab-scale experiments and mini-plant operations (Illner, Müller, et al., 2016a), (Illner, Pogrzeba, et al., 2016b), (Müller, Illner, et al., 2017).

### Reactor

The reaction pressure is set to 15 bar gauge pressure and the reaction temperature is kept constant at 368 K. Depending on the emulsion state the stirring speed is varied between 600 and 1500 rpm to guarantee gassing which ensures sufficient dissolution of synthesis gas in the mixture.

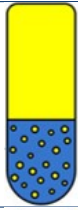


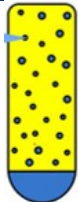
### Settler

According to the discussion given in Section 2.1, four types of phase separation can be found: Two-upper  $\bar{2}$ , two-lower  $\underline{2}$ , single-phase and three-phase (shown in Figure 2.2b). Each phase separation type shows features and/or constraints with respect to the process (see Table 2.1).

Earlier experiments determined that working in regime 3 takes less time for the separation to be completed compared to regime  $\underline{2}$ . So, the operating region of the decanter is defined by the regime 3. Consequently, the residence time in the settler is set to 30 mins and the temperature window necessary to maintain a three phase separation is around 4 K. The concentration ranges of the liquid components derived from plant operation data are shown in table 2.2.

## 2.3. Role of the phase separation model in the optimization framework

Table 2.1: Features of phase separation regimes

Phase Regime		Feature
Two-phase lower regime $\underline{2}$		Since the catalyst is present in the lower phase this regime is convenient for the separation of the product and the recycle of surfactant and catalyst.
Three-phase regime 3		Convenient for the separation of product and the recycle of surfactant and catalyst.
Single phase 1		The homogeneous mixture is suitable for reaction but not for separation purposes.
Two-phase upper regime $\bar{2}$		Despite catalyst is separated from the mixture, the regime is not convenient for separation due to the loss of surfactant in the product phase

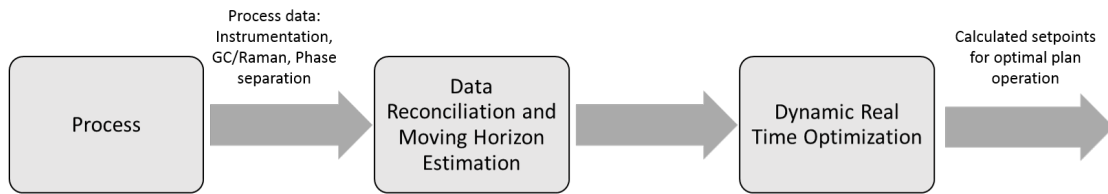
Component	Minimum [wt %]	Maximum [wt. %]
water	40	60
1-dodecene	40	60
surfactant	6	10
1-tridecanal yield	0	40

Table 2.2: Minimum and maximum concentration of liquid components

Further studies need to be carried out to fully comprehend the temperature boundaries of the 3 phase region at different compositions (Kahlweit's fish body).

## 2.3 Role of the phase separation model in the optimization framework

A *chance-constrained dynamic real time optimization (D-RTO)* based framework calculate the setpoints for over twenty regulatory control loops (PIDs) in the process (see Figure 2.6). For this purpose, a data set of measurements is gathered from the plant and validated. Afterwards, the validated measurements are used to refit the model to the current state of the plant to calculate the optimal setpoints for the controllers (Illner, 2014) (Müller, 2015).



**Figure 2.6:** Control strategy at TU Berlin hydroformylation mini-plant

The optimization problem consists of the maximization of the product content (linear aldehyde n-tridecanal) in the outlet stream. Also, the yield and the amount of catalyst and surfactant leaching, which ensures a stable operation of the plant in the three-phase region, must be minimized.

One of the most important parts of every process optimization is the underlying model (Müller, Illner, et al., 2017). In the context of the mini-plant, the model of the process, shown in figure 2.7, is formulated using the platform MOSAICmodelling and consists of 23 process units including liquid hold-ups, 12 compounds, 25 streams and, a compensation for the pipes volumes (hold-up 15 and 16), which is needed to reduce the model mismatch.

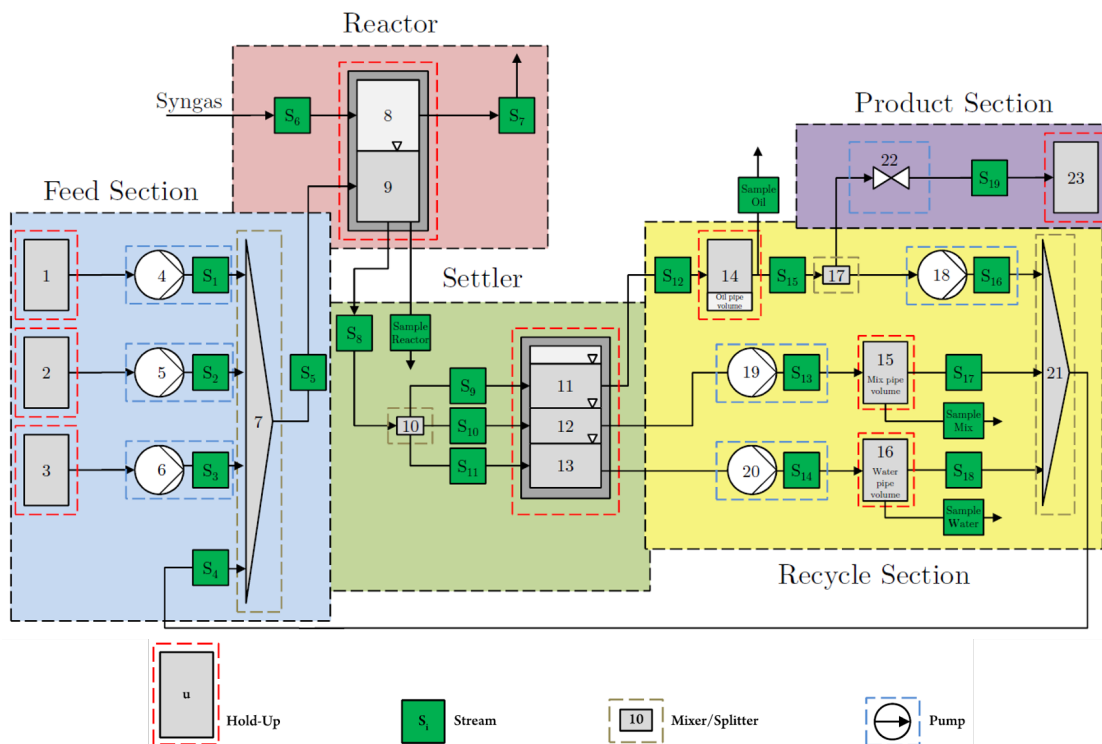


**Figure 2.7:** Scheme of the dynamic model of the mini-plant

The reactor equations contain a total of 20 kinetic parameters that are estimated through maximum likelihood methods. Since the settler unit is of interest for the development of this thesis, a more detailed description about the model is shown in the following section.

### 2.3.1 Settler model

The settler unit is modeled as a single cylindrical tank-unit which holds three liquid phases: oil, mixture and water. The concentrations and split ratios in the splitter, seen in Figure 2.8, depend on the phase separation behavior of the microemulsion. The basic idea of the phase separation model is to have two equations for the volume fractions of oil  $\varphi_{oil}$  and water  $\varphi_{wat}$  depending on the concentrations and temperature of the settler. In the model, the current concentrations from the reactor outlet (stream  $S_8$  in Figure 4.15) are used as inputs for the set of the equations to calculate the ratios in the splitter. However, the temperature and concentrations dependent equations are missing, so the full understanding and description of the phase separation behavior in microemulsions is needed to complete the model.

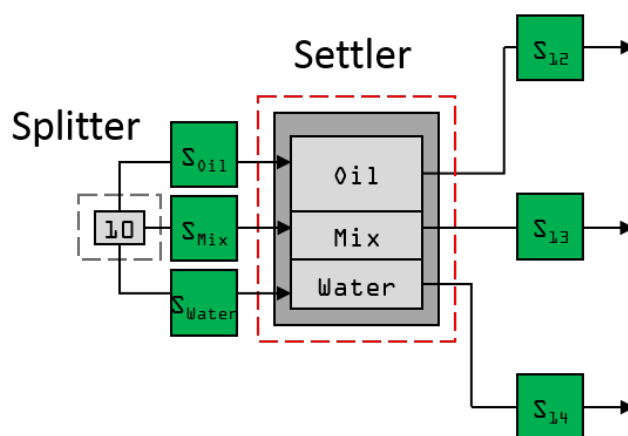


Figure 2.8: Scheme of the separator unit model

Additionally, the 3 phase drains are activated following certain level constraints in the settler. Depending on the level of each of the phases the activation of the outlets is performed. For example, taking a look at the image in Figure 2.9 for the water case, if the water level increases until it passes the height of outlet 2, the outlet 2 and 3 must be activated. If the oil phase is positioned between the outlet 1 and outlet 2, and if it has not reached the outlet 2, only the outlet 1 is activated. If the volume fraction of the middle phase is large, then the three phase separation is lost, so all the outlets are activated to a full recycle mode.

The level switches required for the model elements and streams, are discrete switches. Initially, the use of binary variables was considered, which forms a Mixed Integer Nonlinear Programming MINLP for optimization. However, since these type of switches increase the computational effort of the MINLP solution, the use of sigmoidal functions was encouraged. The sigmoidal switches are continuously performed between 0 and 1 with bounded state transitions, which as consequence, the problem was reformulated as a Non Linear Programmin NLP.

$$Sigmoid = \frac{1}{1 + e^{(argument)}} \quad (2.3)$$

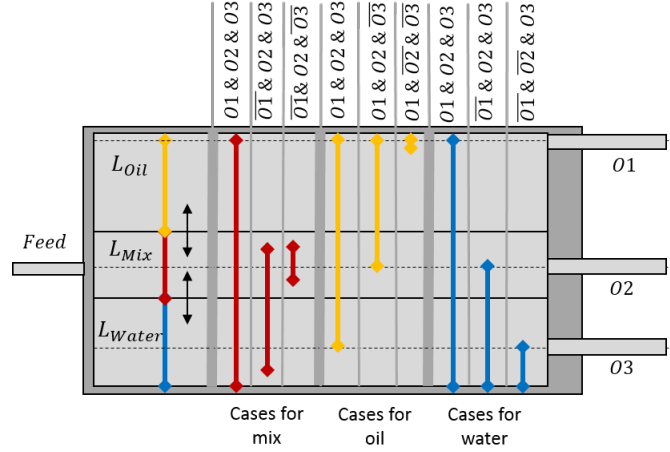


Figure 2.9: Switches for

The sigmoidal switch argument must be carefully defined because a large steepness or slope leads to non differentiability while a too gradual one results in an improper switch.

## 2.4 Overview of the proposed solution

According to the problem stated at the beginning of this Chapter, the estimation of the surfactant concentration in the settler can be obtained automatically if the three phase separation behavior is modelled and if the information about the actual state of separation inside the settler (i.e. the level of the phases) is acquired.

The general solution to the problem is sketched in Figure 2.10. First, the temperature  $T$  and conversion  $X$  measurements are obtained through the instrumentation available at the mini-plant (see subsection 2.2.2). A web camera positioned in the settler provides the images corresponding to the actual separation state. These images need to be captured and analyzed automatically with an ad hoc image processing algorithm to detect the level of the phases and provide the volumetric fractions  $\varphi_i$  of each phase. And more specifically, since the sum of the volume fractions  $\varphi_{oil}$ ,  $\varphi_{surf}$  and  $\varphi_{wat}$  is 100 %, only the volume fractions of oil and water are used for the development of the model. The field information is used as an input of the soft-sensor, in order to estimate the surfactant and oil-to-water ratio, and to provide a suitable operating region for the operator.

In this thesis, parameter identification techniques are used to identify the static relationship between the volumetric fractions  $\varphi_{oil}$ ,  $\varphi_{wat}$ ,  $T$ ,  $X$  and the values of  $\alpha$  and  $\gamma$ . In particular, black-box models are investigated.



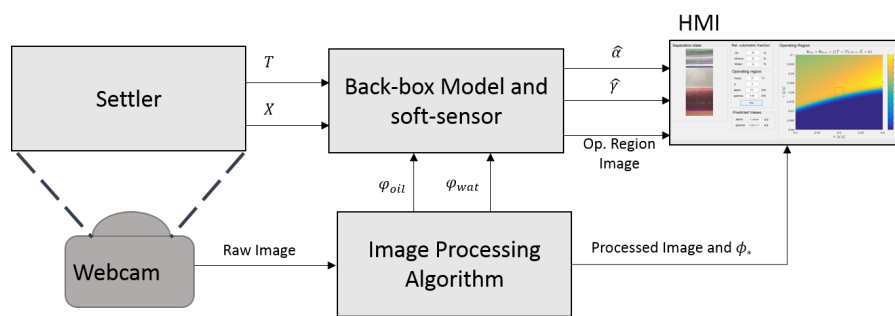


Figure 2.10: Overview of the general solution



# Chapter 3

## Image Processing Algorithm for Phase Level detection

### 3.1 Image processing

The principal concepts used in the image processing algorithm for the phase level detection are described. In particular, color spaces, image filtering and edge detection are discussed.

#### 3.1.1 Color spaces

The suitable solution for the level detection algorithm is based on color segmentation due to the diversity of the color properties of the phases. An appropriate selection of the working color space is the key to ensure their correct detection. For this reason, a review of the most used color spaces for image detection is presented.

There are different color representations in image processing applications. The gray-scale value, for example, represents the amount of incoming light or intensity of a pixel and it is denoted by a single 8-bit value, obtaining 256 shades of gray. On the other hand, when dealing with color images, RGB color space represents a pixel of color with 3 values. Each value represents the amount of incoming red, green and blue light. Typically, the color pixel is represented by a 8-bit 3-dimensional vector (see equation (3.1)), meaning that 256 different shades of each color can be obtained.

$$\text{Color pixel} = [\text{Red, Green, Blue}] = [R, G, B] \quad (3.1)$$

However, from the human perception, the RGB representation is not intuitive (Moeslund, 2012). When perceiving the color, a human uses the notion of *hue* and *saturation*. The hue is the dominant wavelength in the perceived light and represents the pure color. The saturation represents the amount of white light mixed with the pure color. Figure 3.1 shows the hue-saturation relationship, where the hue value is defined as an angle  $\vartheta$  (range from  $0^\circ$  to  $360^\circ$ ) and the saturation is the distance from the center (range from 0 to 1). For example, hue =  $0^\circ$  means red

and saturation will indicate how much intensity of the red color there is.

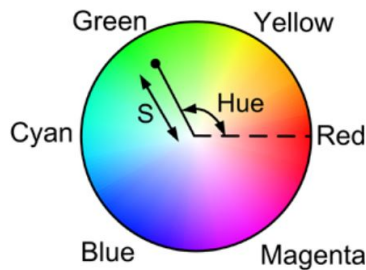


**Figure 3.1:** The hue-saturation representation. Image taken from Moeslund, 2012

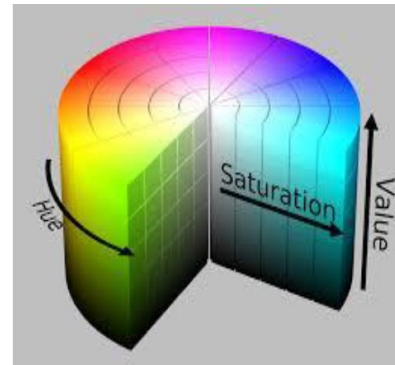


**Figure 3.2:** The HSV color space representation. Image taken from Bora et al., 2015

HSV (Hue, Saturation, Value) space color (see figure 3.2), for example, uses the hue-saturation representation mentioned previously, but an extra channel called *value* is used. The latter ranges from 0 to 1 and corresponds to the amount of black in a color.

Other color representation exist: CMY, YCbCr, CIE L\*a\*b, CIE L\*U\*V. However grey-scale, RGB, CIE L\*a\*b HSV color spaces are most often applied in image processing. Besides, as mentioned in Ibraheem et al., 2012, HSV color space is suitable for image processing applications, including color detection, since it is device independent and it is more robust with external light changes.

For more information about other color spaces, please refer to Ibraheem et al., 2012 and Moeslund, 2012.

### 3.1.2 Image Filtering

Since color and edge detection methods are easily affected by image noise, an appropriate filter of the noise is needed to prevent the false detection. Two types of filters are discussed in this section.

#### Gaussian Filter

The Gaussian filter is one of the simplest methods used to smooth or blur an image. The value of a pixel of the filtered image (or output image) is calculated by estimating a weighted average of intensities of the adjacent pixels. In other words, the output image is the result of the convolution with the input image and the 2D *Gaussian function* or *Gaussian kernel* (Paris et al., 2009).

$$G_{\sigma}(x, y) = \frac{1}{2\pi\sigma^2} \cdot e^{-\frac{x^2+y^2}{2\sigma^2}} \quad (3.2)$$

where  $\sigma$  is the standard deviation which defines the neighborhood size,  $x$  and  $y$  are the two directions of the pixels. The more neighbors included, the more strongly the image is filtered.

As seen in equation (3.2), the Gaussian convolution only depends on the distance of the pixels of the image and not in the content. This leads to an image with blurred edges, since the pixels across discontinuities (bright and dark) are averaged together.

### Bilateral Filter

A solution for preserving the edges while filtering an image is proportioned by the *bilateral filter*. This filter is based in the Gaussian filter, but it does depend not only on the distance of the adjacent pixels, but also on the intensity differences (Paris et al., 2009). However, a main disadvantage is their large computational cost. This effect can be mitigated by applying the bilateral filter iteratively.

### 3.1.3 Edge detection

In many industrial applications, image processing is used to measure dimensions of objects. Therefore, it is very important to detect its contour. An edge in an image is defined as the position where a significant change in gray-level values occurs (Moeslund, 2012). This change can be detected using the values of two gradients:  $G_x$  i.e; the gradient in the  $x$  direction and  $G_y$  i.e; the gradient in the  $y$  direction. The magnitude and the direction of the resulting gradient is defined as:

$$G = \sqrt{G_x^2 + G_y^2} \quad (3.3)$$

$$\Theta = \arctan\left(\frac{G_y}{G_x}\right) \quad (3.4)$$

The gradients  $G_x$  and  $G_y$  can be computed by using the differential operator method (y. Zheng et al., 2010). Differential operators can be divided in two types: First-order operators like the Sobel operator, the Prewitt operator and the Roberts operator, and Second-order operators which include the LOG operator and the Canny operator. For the development of this project, the Sobel operator and the canny operator have been investigated.

The Sobel operator, for example, uses 3x3 kernels, which are convolved with the original image to calculate the approximations of the derivatives as follows:

$$G_x = \begin{bmatrix} -1 & 0 & +1 \\ -2 & 0 & +2 \\ -1 & 0 & +1 \end{bmatrix} \otimes A \quad (3.5)$$

$$G_y = \begin{bmatrix} -1 & -2 & -1 \\ 0 & 0 & 0 \\ +1 & +2 & +2 \end{bmatrix} \otimes A \quad (3.6)$$

In (3.5) and (3.6)  $A$  is the gray-level information of the input image.

On the other hand, calculating the gradients with Canny operator is more complex to achieve. First, a Gaussian filter is needed to smooth the image, then some first-order kernels are used for the estimation of the gradient intensities. Next, the *non-maximum suppression* technique is used for thinning the edges after smoothing. Finally, a thresholding method is used to filter weak gradient edges (Canny, 1986).

It is important to highlight that first-order operators result in wide edges and are very sensitive to noise. This effect is even stronger in second-order operators. The selection of the proper method for edge detection highly depends on the environmental conditions. In the next sections, the application of the previously studied concepts in the solution for the phase level detection are described.

## 3.2 Phase level detection: main steps

The decanter used in the TU Berlin miniplant is composed by a sight glass which allows the inspection of the actual state of the phase separation. A high resolution web camera (1920x1080 pixels) takes a picture every second of the settler's state and stores it in the server every 30 minutes. The system is surrounded by a dark plastic cover to avoid undesired reflections of external lights. A little inspection hatch in the cover can be opened so that the operator may visualize the actual state of the phase separation.

Once the picture is taken and stored successfully, the image processing script, programmed in c++ using OpenCV library, automatically detects the level of each phase: Oil, mixture, water and foam (if present). The flow chart of the algorithm and the result of the program is shown in figure 3.3.

As a first step, the stored image is read from the script and decomposed in a matrix which contains the BGR scale values of each pixel. Since the original picture shows also surrounding objects, it is necessary to crop the image to the Region of Interest (ROI), which facilitates and accelerates the further processing steps.

According to Figure 3.4, the original image is decomposed in a matrix, whose coordinates  $(x, y)$  define each pixel's position along a global frame  $(x^G, y^G)$ . Once the ROI is obtained, the position of the pixels will be referenced to a new set of coordinates  $(x^L, y^L)$ . This change of frame needs to be taken into account for all further cropping procedures.

Afterwards, the cropped image is filtered to reduce the noise and to preserve the edges formed between the phases. According to the discussion of types of filters in subsection 3.1.2, a bilateral filter would be more appropriate for level detection. However, a great disadvantage of the filter is not only in its high computational cost, but also in the preservation of some undesired edges formed by outer light reflections, which results in an erroneous level detection. Therefore, the most

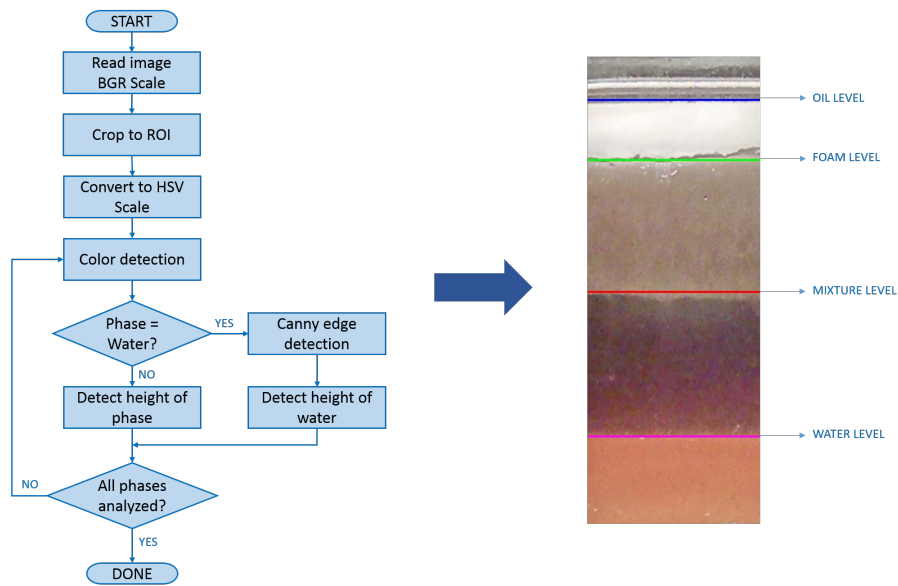


**Figure 3.3:** Flow diagram of image processing script for phase level detection

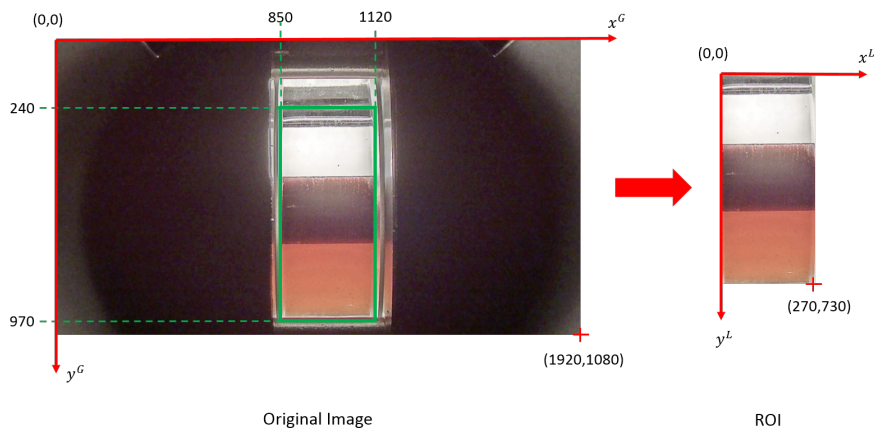


**Figure 3.4:** Original image cropped to Region of Interest

suitable filter applied to smooth the images was the Gaussian Blur with 3x3 kernel. A bigger kernel size would smooth the image even more, but it would result in the loss of definition of the edges. For this reason, the 3x3 kernel was selected in order to balance a light smooth with the preservation of the edges.

Once the cropped image is filtered, the resulting image is converted to HSV color space to proceed with color detection. As explained in Section 3.1.1, the HSV space color is suitable for image processing with changing light environments. In this case, the hatch that covers the sight glass and the camera is opened constantly due to the periodical inspections by the operators.

### 3.3 Color detection

Color detection is one of the most important tasks in image processing applications. It consists of searching a piece of an image that contains pixels of a specific color. This method is convenient for phase-level detection considering that the colors of the phases present in the settler are different. Besides, when the reaction is activated with Syngas, the color of the phases change from red-like color to yellow-like color. These properties can be exploited again with a suitable selection of the new colors thresholds.

Performing the color detection of each phase, needs the correct definition of its own color threshold, which means that oil, foam, mixture and water are each characterized by a specific color range. Using a threshold for detection (instead of one single color) is essential because noise, changes of light, phase composition, bubbles, etc., causes that all image pixels that belong to the same phase may have slightly different colors, but within the same range.

For this purpose, a program is created using openCV in which 6 photos of the decanter state taken from different experiments and dates are uploaded. The pictures are selected to ensure the diversity of states in order to find a threshold that better fits different scenarios. Then, the images are converted to HSV space color and, with the help of tracking bars, the upper and lower value for each channel (Hue, Saturation, Value) are changed until the selected phase is masked and isolated from the other ones (as shown in figure 3.5). Oil, for example, has HSV values: H: 0-37, S: 0-52, V:171-255 for all 6 pictures. This range allows to completely isolate the phase from others. However, the ranges of foam, water and mixture do not completely isolate the phase. This effect can be seen in Figure 3.5d, where water is detected also at middle phase location. To reduce this problem as much as possible, the combination of color detection, of cropping procedures and of canny edge detection is used.

### 3.4 Boundary detection

Once the adequate HSV thresholds are chosen, the detection of the boundaries of each phase is done in the next order: Oil, water, emulsion and foam. The next algorithm provides the steps followed to achieve this goal:

1. Convert image from BGR to HSV space color.
2. Mask or isolate the phase using the HSV thresholds found with the color detection method (Table 3.1).
3. Perform morphological operations such as erosion and dilation. This transformations help to eliminate undesired dots and close holes.
4. Use canny edge detection to detect the edges of the masked phase. (See subsection 3.1.3).



5. Find contours associated with the Canny edges and fit them into a rectangle. Then, select the one with the highest area. The boundaries of this polygon are the boundaries of the phase.
6. Eliminate the portion of the phase found on the original picture and use it for the next phase detection.

**Table 3.1:** Example of steps in level detection algorithm

Phase	1.	2.	3.	4.	5.	Result
Oil						
Water						
Mixture						
Foam						

As shown in Table 3.1, the level of water obtained only by using the color detection method is not accurate due to the similarity of colors between emulsion and water around the boundaries. To overcome this problem, another method is added for water phase level recognition. It consists in applying a canny edge detection algorithm with 3x3 kernel to the full image and find the borderline between mixture and water.

To do so, it is necessary to convert the image from BGR scale to gray scale (see Figure 3.6). Then, Canny edge detection is performed and the contours associated with them are found. To obtain the horizontal lines related to those contours, the Hough Line Transform is applied, which is a technique used to detect any shape in mathematical form. In this case, the shapes of interest are the horizontal contours that define the boundaries between water and middle phase.

After all boundaries of phases are detected, the superior limit is taken as the level of the phase. However, all levels are in terms of pixels, which is not a useful unit for control purposes. The most suitable unit is volume fraction and needs to be calculated by knowing the dimensions of the decanter.

### 3.5 Conversion from level to volumetric fraction

To be able to use the output of the image processing algorithm and the obtained model for the soft-sensing of the surfactant concentration, the image processing output must be the volumetric fraction of each phase: Oil, foam (if existent), surfactant and water.

The volume of a fluid contained in a horizontal cylindrical vessel as function of its level can be computed as follows:

- If the level of the fluid is above the center, then the volume is given by:

$$V_l = L \cdot \left( \pi R^2 - R^2 \arccos \left( \frac{R - h_1}{R} \right) + (R - h_1) \sqrt{2Rh_1 - h_1^2} \right) \quad (3.7)$$

where  $V_l$  is the volume of the fluid,  $L$  and  $R$  are the length and radius of the cylinder,  $h_1$  is the distance from the top of the vessel to the surface of the liquid.

- If the level of the fluid is below the center, then the volume is given by:

$$V_l = L \cdot \left( R^2 \arccos \left( \frac{R - h}{R} \right) - \sqrt{R^2 - (R - h)^2} \right) \quad (3.8)$$

where in this case  $h$  is the level of the fluid.

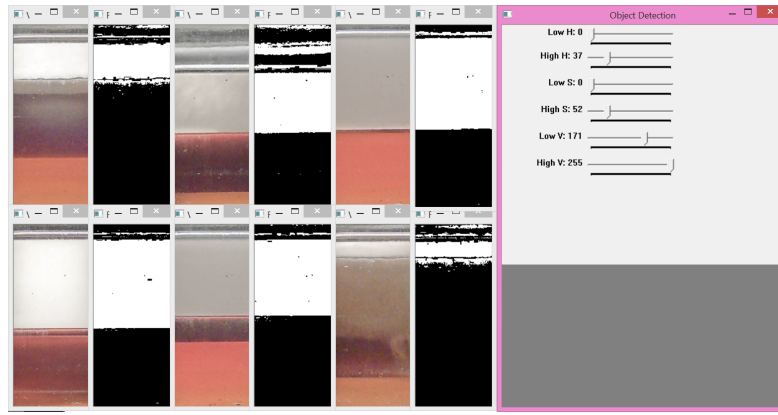
Calculating the volumes of all the phases contained in the settler by using the level information, the volumetric fractions  $\varphi_i$  are just simply a relation between the phase volume  $V_{phase}$  and the total volume  $V_{tot}$ , as shown in the following equation:

$$\varphi_i = \frac{V_i}{V_{tot}} 100 \quad (3.9)$$

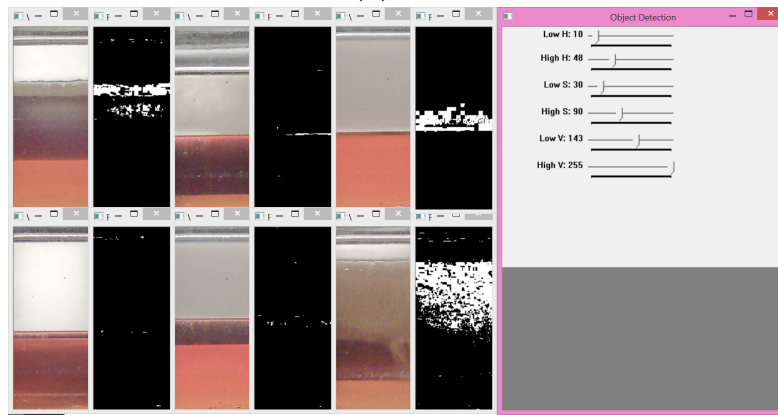
The volumetric fractions are the outputs of the image processing algorithm which are saved in a .txt file. From the moment the image is read until the .txt file is written, an average processing time per picture is 1.5 seconds has passed. This file is taken as an input for the soft-sensor of surfactant concentration and oil to water ratio. The integration of the model and image processing algorithm in the control system is discussed in the next chapter.

### 3.6 Cases of success and failure

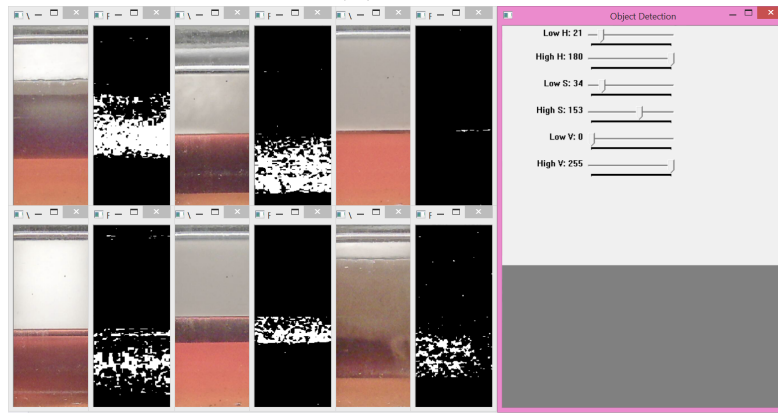
The automatic image processing algorithm was tested in 1000 images obtained from previous plant operations. Around 76 % of the images were successfully evaluated, including images that show a light surfactant buildup in the sightglass, as seen in Figure 3.7a. For images where the surfactant buildup is large (Figure 3.7b), the level detection algorithm fails and only water level is correctly detected. Additionally, Figure 3.7c shows a failure in the detection of the water level, due to a random strong edge formed by light reflection in the sightglass.



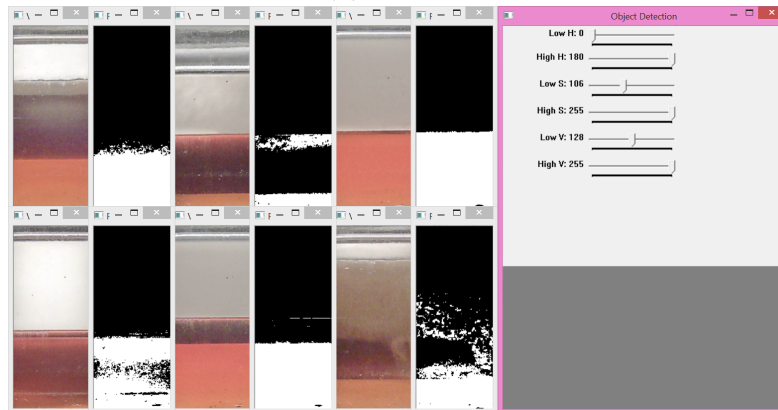
(a) Oil



(b) Foam



(c) Emulsion



(d) Water

Figure 3.5: Threshold definition for all phases

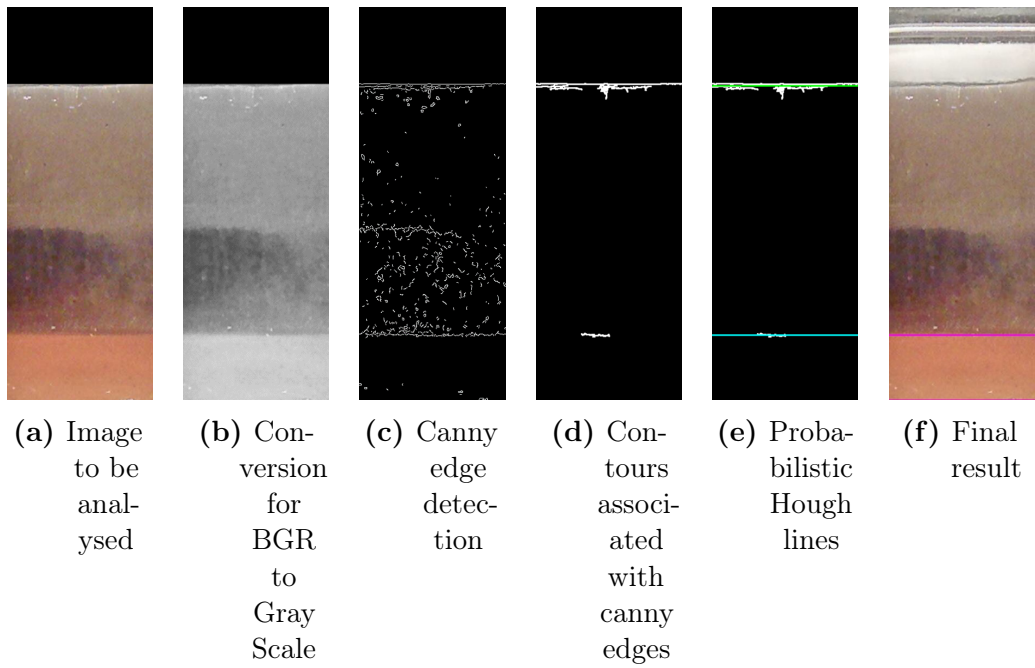


**Figure 3.6:** Example of water level recognition using canny edge detection

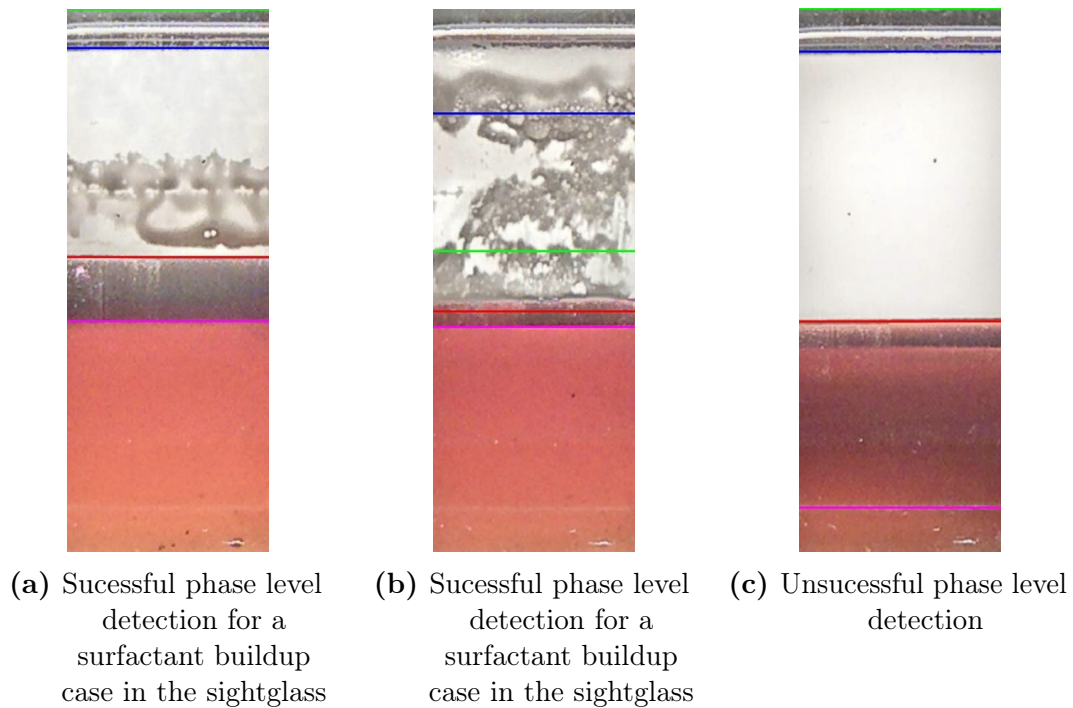


**Figure 3.7:** Successful and failure cases in the level detection algorithm



# Chapter 4

## Experimental design and black-box modelling of the phase separation process

### 4.1 General Methodology for Identification

Many industrial processes need to be operated safely and efficiently. For this aim, a suitable controller is needed, which is designed based on a model that best represents the process. These models can be constructed from physics laws and balance equations. Nonetheless, when the processes are so complex that it is not possible to obtain reasonable models using only physical insight, system identification techniques must be applied.

System identification is a modelling approach based on data obtained with suitable experiments performed on the process. These data are used to estimate the values of the unknown parameters of the selected model classes. Models obtained through system identification are valid only for a certain working point, or for certain value ranges. However, in most of the cases, although the model lacks a direct physical meaning, it contains a good description of the system's behavior.

The general methodology for system identification, as shown in Figure 4.1, starts with the design and execution of the experiments in which the system is excited with an input signal and its response is observed over a time interval. These data are then collected and stored for their further analysis. An appropriate model structure must be selected to fit the input and output sequences and, using statistically well grounded method, the unknown parameters of the model can be estimated. Once the model and its parameters are obtained, it is necessary to test it to corroborate if it is an appropriate representation of the system. If this is not the case, then another form of model must be considered and the estimation and validation process has to be performed iteratively (Soderstrom and Stoica, 1989).

Following the above sketched system identification methodology, the static experimental model of the phase separation behavior in microemulsions is obtained.

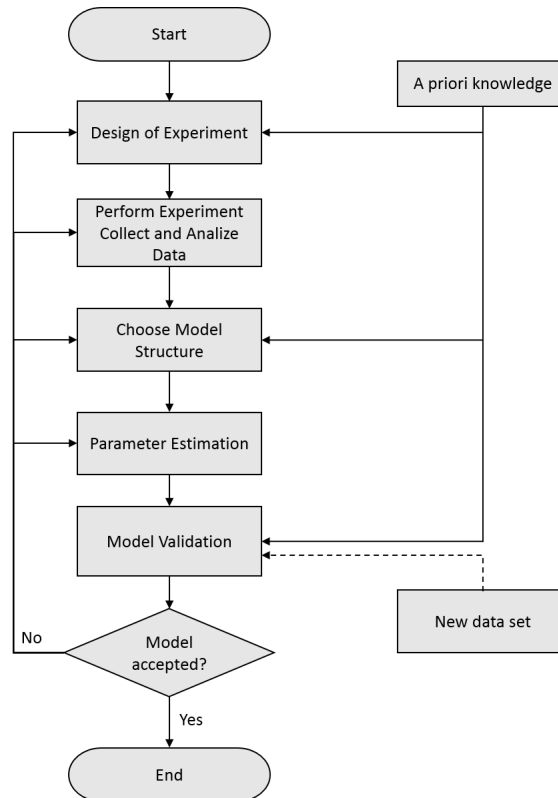


**Figure 4.1:** Flow Chart of system identification methodology. Redrawn from [Soderstrom and Stoica, 1989](#)

More specifically, the following steps are carried out, each described in a dedicated section: Experimental design, data analysis, model structure selection, parameter estimation, and model validation.

## 4.2 Experimental Design

### 4.2.1 The a-priori knowledge of the system and variables of interest

According to the a-priori knowledge about the phase separation in microemulsions, it is known that the state of the separation depends strongly on the temperature and the concentrations of the components. The components that form the microemulsion under study are: feedstock oil 1-dodecene, 1-tridecanal aldehyde, surfactant marlipal 24/70 and catalyst solution with rhodium based precursor. More specifications about the components can be found in the Section 2.2.3. For simplicity the 1-dodecene and 1-tridecanal will be referred as the oil phase or *top phase*, the surfactant rich phase will be called *middle phase* and the catalyst solution will be referred to as *water phase* or *bottom phase*.

The target is to study the three phase separation region evolution. More specifically, the aim is to obtain obtain a model that describes the relationship



between the volume fractions  $\varphi_{oil}$  and  $\varphi_{wat}$  and the following variables:

- Temperature  $T$  [°C]: Temperature of the mixture.
- Oil-to-water ratio  $\alpha$  [g/g]: Mass fraction of the oil in the mixture of oil and water. Defined in equation (2.1).
- Surfactant concentration  $\gamma$  [g/g]. Defined in equation (2.2).
- Conversion  $X$  [g/g]: Describes how much of the aldehyde 1-tridecanal has been formed.

$$X = \frac{m_{tdc}}{m_{dod}} \quad (4.1)$$

where  $m_{tdc}$  and  $m_{dod}$  are the masses of 1-tridecanal and 1-dodecene respectively.

The obtained model will be used to complete the general mini-plant model described in Section 2.3. To estimate the surfactant concentration and oil-to-water ratio, the equations of the model are solved for  $\alpha$  and  $\gamma$ , based on the actual state of separation in the settler represented by  $\varphi_{oil}$ ,  $\varphi_{wat}$ ,  $X$  and  $T$ . The volume fractions  $\varphi_{oil}$ ,  $\varphi_{wat}$  are computed as follows:

$$\varphi_i = \frac{h_i}{h_{oil} + h_{surf} + h_{wat}} 100 \quad (4.2)$$

where  $i$  represents the oil, surfactant and water phases,  $h_i$  represents the level of the phases obtained with the image processing algorithm described in Chapter 3, and  $\varphi_i$  is the relative level of the phase or volume fraction in terms of percentage.

Keeping into account the Kahlweit's fish diagram shown in figure 2.2b, the three phase region, which is the "body of the fish", is delimited by an upper temperature  $T_h$  and lower temperature  $T_l$ . These boundaries change with respect to the composition of the mixture, so they are also a function of  $\alpha$ ,  $\gamma$  and  $X$ .

Preliminary studies performed in the mini-plant at  $X = 0$  [g/g] showed that when the mixture is in the three phase region and temperature decreases until the boundary with the  $\underline{2}$  region without changing the concentrations of the components, two behaviors can be seen. The first one is characterized by the formation of a dense surfactant rich layer (further referred to as "foam") between the middle phase and top phase, and a decrease of the water phase level. A similar behavior occurs in the transition of the three phase regime and the  $\bar{2}$  regime, but in this case the white foam block appears between the middle and bottom phase and/or the oil phase level decreases considerably (see Figure 4.2).

This a-priori knowledge was used in the design of the experiments. The setting is explained in the next subsection.

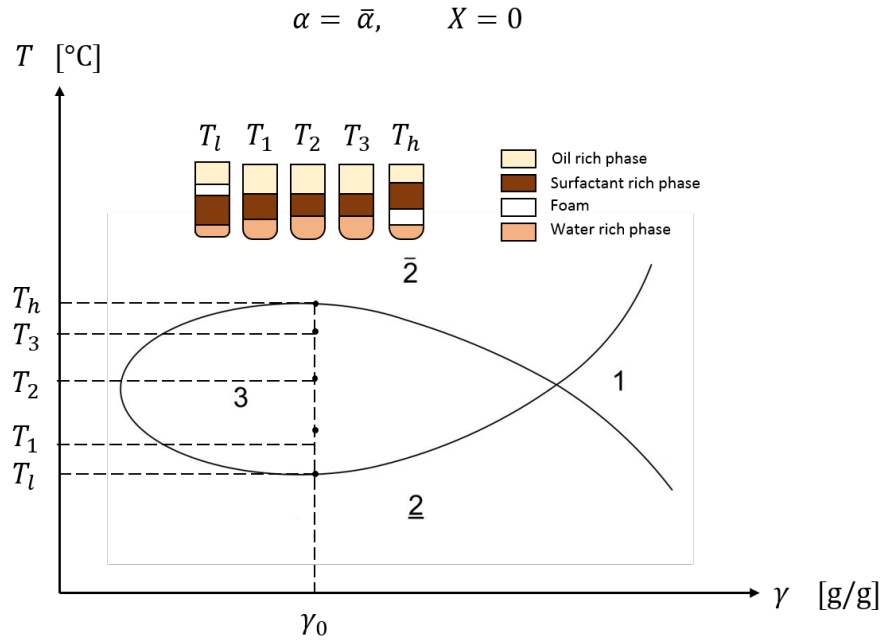


**Figure 4.2:** Three phase separation of the mixture at different temperatures and a constant concentration of surfactant  $\gamma = \gamma_0$

## 4.2.2 Experimental setting

The experiments were performed in the laboratory using the following elements:

1. Thermostat
2. Jacketed vessel
3. Magnetic stirrer
4. Thermometer with Pt100 probe
5. Camera and tripod.
6. Components: 1-dodecene, Marlipal 24/70, rhodium based catalyst solution and 1-tridecanal. The latter is added to the mixture to emulate a conversion value  $X$  different from zero.

In Figure 4.3 the set-up for the experiments is depicted. A thermostat with water is connected to a jacketed vessel which contains the emulsion formed with the components. A magnetic stirrer mixes the mixture and the Pt100 probe is inserted inside the vessel to measure the temperature of the mixture.

## Experimental procedure

The preliminary phase consists of the preparation of the samples. More specifically, for a desired composition (previously fixed) of  $\alpha = \alpha_{sp}$ ,  $\gamma = \gamma_{sp}$  and  $X = X_{sp}$ , the masses of each component  $m_{dod}$ ,  $m_{surf}$ ,  $m_{cat}$  and  $m_{tdc}$  are calculated to meet those concentrations. The component masses are measured with an analytical

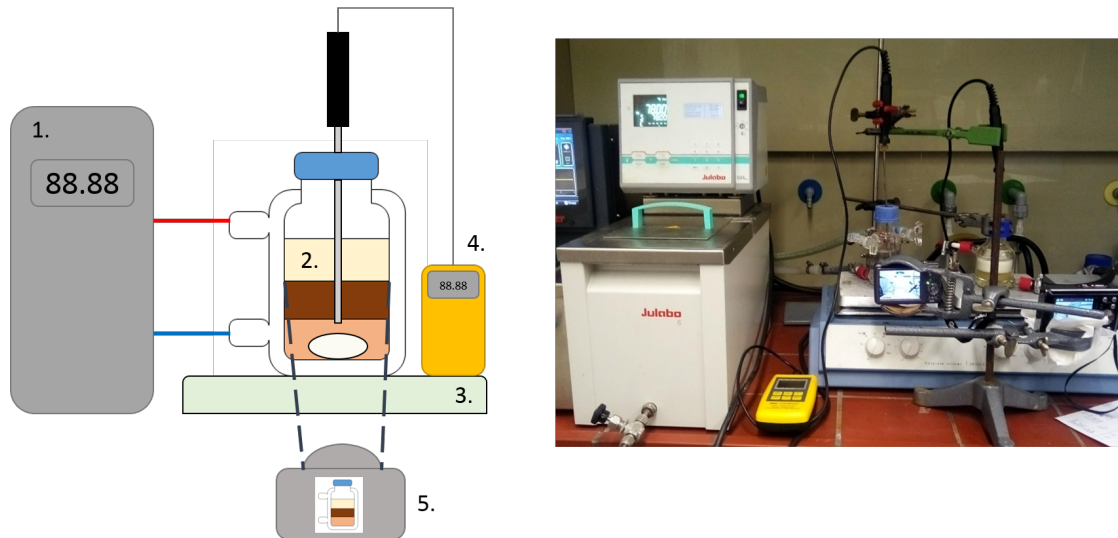


**Figure 4.3:** Schematic and real set-up of the experiments. 1. Thermostat, 2. Jacketed vessel, 3. Magnetic stirrer, 4. Thermometer with Pt100, 5. Camera and tripod

balance and introduced inside the vessel together with the magnet of the stirrer. Since the components are sensitive to oxygen, the vessel must be inertized with nitrogen before its closure and be very well sealed during the experiment. Once the samples are prepared the next procedure must be followed:

1. Connect the input and output of the jacket of the vessel to the input and output of the thermostat.
2. Insert the pt100 probe inside the vessel.
3. Introduce the temperature set-point in the thermostat at  $T_{sp}$  to heat the mixutre.
4. Mix the emulsion for 10 minutes or until the internal temperature is in equilibrium.
5. After 10 minutes of stirring, stop the mixing, measure the initial temperature of the mixture.
6. Record a video during 30 minutes.
7. Repeat for at least 5 different temperature values that includes the upper and lower boundaries, and at least 3 different temperature values inside the 3 phase region.

The key to perform the experiments is to find first the thermostat temperature  $T_{sp}$  at which the three phase separation region begins. Initially, this was done by trial and error until the behavior described in the Section 4.2.1 was seen. After having enough experience and enough data to form an initial model, the approximately temperature boundaries of the three phase region were estimated and set as initial experiment.

### 4.3 Experimental observations

Concerning experiments performed with concentrations  $\alpha = \bar{\alpha}$ ,  $\gamma = \bar{\gamma}$ ,  $X = 0$  and variable temperatures  $T$ , the emergence of the white foam was observed in the lower and upper boundary of the three phase region. An example can be seen in Figure 4.4e, related to the experiment  $\alpha = 0.5$ ,  $\gamma = 0.075$ ,  $X = 0$ , where the three phase region starts at temperature  $T = 76^\circ\text{C}$ . Foam is observed between the upper and middle phase, and the levels of water phase is small. As the temperature increases, the foam disappears and the level of oil and water increases and maintains until reaching  $T = 83^\circ\text{C}$ , where foam is observed again between the middle and lower phase, and oil level starts decreasing. At temperatures larger than the upper boundary, the three phase separation is lost.

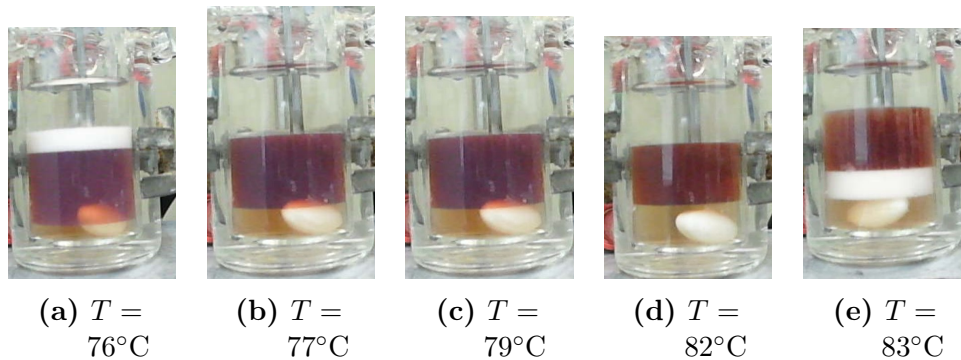


**Figure 4.4:** Phase separation evolution for variable temperatures and concentrations  $\alpha = 0.5$ ,  $\gamma = 0.075$ ,  $X = 0$

Regarding the experiments performed with concentrations  $\alpha = \bar{\alpha}$ ,  $\gamma = \bar{\gamma}$ ,  $X = \bar{X}$  and variable temperatures  $T$ , there was not foam formed in the three phase region boundaries. As shown in Figure 4.5f, the three phase region starts when the temperature increases from 78 to 80 °C. As the temperature increases, the oil phase changes from clear to turbid ( $T = 85^\circ\text{C}$ ), and starts decreasing until the three phase separation is lost at  $T = 87^\circ\text{C}$ .

Experiments in which the color base of the mixture changed from red to yellow, as shown in figure 4.6, were discarded. This means that the mixture was in contact with oxygen and the repeatability of the experiment could not be ensured anymore.

#### 4.3.1 Sources of error

The temperature of the mixture was changed through the heating jacket connected to the thermostat. However, only the temperature of the thermostat was controlled, and not the internal temperature of the mixture. This implies, that along the 30 minutes of the experiment's duration, the temperature of the mixture decreases. Since only the initial temperature was considered, the changes in the phase separation behavior caused by temperature gradient is unquantifiable.

For some experiments, the addition of the surfactant directly on the vessel was done using a syringe. Drops of the surfactant could fall on the cap of the vessel

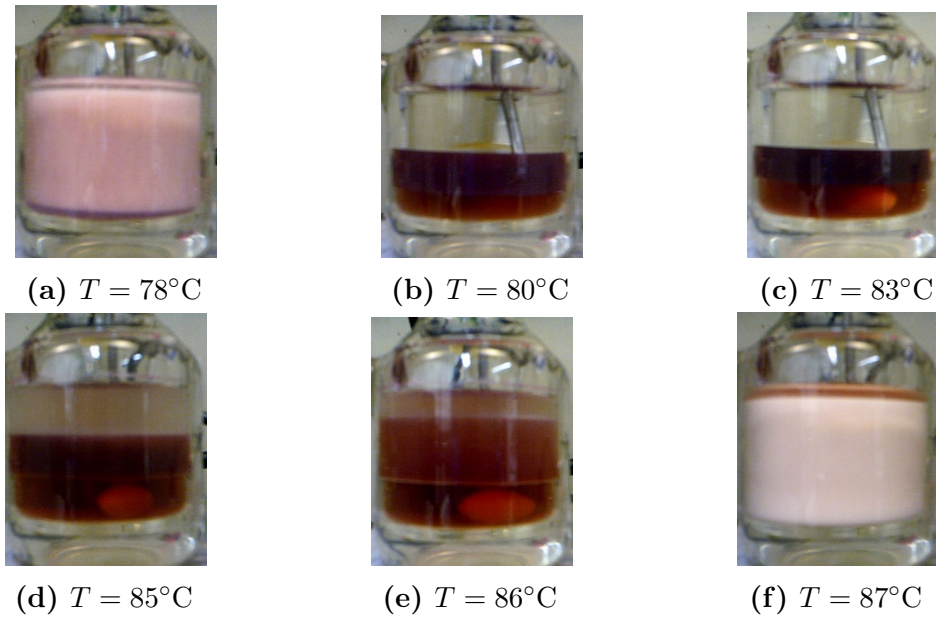


**Figure 4.5:** Phase separation evolution for variable temperatures and concentrations  $\alpha = 0.5$ ,  $\gamma = 0.07$ ,  $X = 0.2$



**Figure 4.6:** Discarded experiment with concentrations  $\alpha = 0.4$ ,  $\gamma = 0.085$ ,  $X = 0.4$  and  $T = 69^{\circ}\text{C}$

and not inside of it. This error is unquantifiable and can cause a significant bias due to the high sensitivity of the phase behavior with respect to the surfactant.

Additionally, the magnet of the stirrer and the stem of the pt100, which are immersed in the mixture, cause a volume displacement of the phases and consequently an error in the definition of the phases level. The volume correction for this case is described in subsection 4.4.1.

## 4.4 Collection of Data

Since the phase separation behavior of every experiment is recorded in a video of 30 minutes, it needs to be converted to \*JPG pictures with a sampling time of 5

seconds. Then, every picture is analyzed semi-automatically, and the information about the relative levels of the three phases is obtained.

The relative levels of the oil, surfactant rich and water phase are calculated as shown in the picture 4.7 and the equations (4.2).

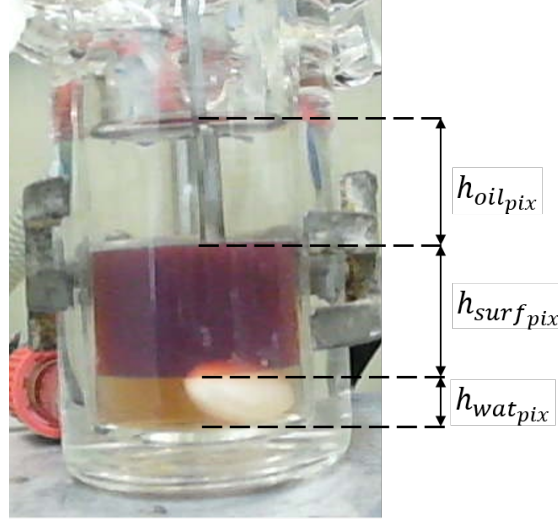


**Figure 4.7:** Determination of the relative level of the phases:  $h_{oil_{pix}}$ ,  $h_{surf_{pix}}$ ,  $h_{wat_{pix}}$  in terms of pixels.

#### 4.4.1 Volume corrections

The phase levels obtained through the analysis of every picture are in terms of pixels, which are not useful for the correction of the volume. It is necessary to calculate the values of the levels in SI units to be comparable with the volume of the magnet in ml. With the information of the relative level of the phases obtained from the pictures  $\varphi_{oil}$ ,  $\varphi_{surf}$ ,  $\varphi_{wat}$  (equations (4.2)) and the density functions of every component, the total volume in ml of the mixture and the volume fractions of every phase can be calculated as follows:

$$V_{tot} = \frac{m_{dod}}{\rho_{dod}} + \frac{m_{tdc}}{\rho_{tdc}} + \frac{m_{surf}}{\rho_{surf}} + \frac{m_{cat}}{\rho_{cat}} \quad (4.3)$$

$$h_i = V_{tot} \frac{\varphi_i}{100} \quad (4.4)$$

where the density of every component  $\rho_{dod}$ ,  $\rho_{tdc}$ ,  $\rho_{surf}$  and  $\rho_{cat}$  is calculated as shown in Appendix A.

Once the volume of the mixture is found, the total level and the level of every phase in millimeters can be calculated with the dimensions of the vessel as follows:

$$h_{tot} = \frac{V_{tot}}{A_v} 1000 \quad (4.5)$$

$$h_{oil} = h_{tot} \frac{\varphi_i}{100} \quad (4.6)$$

where  $A_v$  is the area of the vessel which is a vertical cylinder.

The bottom phase and the middle phase levels analyzed with the pictures are not the correct values because the magnet of the stirrer is immersed in the vessel. This causes a displacement of the volume of the phases. To correct these values, a function  $V_{mag} = f(\%_{coverage})$  is created in MATLAB<sup>®</sup> to calculate the volume in ml of the magnet depending on the percentage of coverage. The volume of the magnet is calculated depending on the percentage of coverage by the water phase:

$$wat_{coverage} = \frac{h_{wat}}{h_{mag}} 100 \quad (4.7)$$

$$V_{wat_{corr}} = V_{wat} - f(wat_{coverage}) \quad (4.8)$$

$$V_{surf_{corr}} = V_{surf} - (f(100) - f(wat_{coverage})) \quad (4.9)$$

$$(4.10)$$

where  $h_{mag}$  is the total height of the magnet, and  $V_{wat_{corr}}$  and  $V_{surf_{corr}}$  are the corrected volumes of the water phase and surfactant phase respectively.

Finally, the corrected relative values of the levels  $\varphi_{oil_{corr}}$ ,  $\varphi_{surf_{corr}}$ ,  $\varphi_{wat_{corr}}$  are:

$$V_{tot_{corr}} = V_{oil} + V_{surf_{corr}} + V_{wat_{corr}} \quad (4.11)$$

$$\varphi_{i_{corr}} = \frac{V_i}{V_{tot_{corr}}} 100 \quad (4.12)$$

A portion of the Pt100 stem is immersed in the mixture and its volume influences the level of the phases. However, the displacement of the phase levels caused by the stem is at most 1 mm. For wider vessels also used in the experiments the pt100 influence is even smaller. This influence is not considered for volume correction due the fact that the heights of the phases are determined manually and 1 mm difference is hardly detected in the picture by the human eye.

## 4.5 Preliminary analysis

For a better understanding about the influence of the independent variables in the phase state separation, two different analysis were carried out and used for the selection of an appropriate model structure. The data used in the following analysis correspond to the data of the three phase separation equilibria. In other words, the data analyzed correspond to the steady state conditions of the phase separation achieved after 30 minutes.

### 4.5.1 Relative phase level vs. temperature

One of the most important relationships that need to be understood is the influence of temperature in the oil and water level. This influence is useful to bound the operating conditions for a stable three phase separation.

Figure 4.8 shows the phase separation state for different temperatures of one experiment carried out with concentrations  $\alpha = 0.5$ ,  $\gamma = 0.080$  and  $X = 0$ . At the boundaries of the three-phase region, the presence of foam was noticeable, but its level is considered to be part of the middle phase. Clearly, the oil and phase water levels decrease when approaching to the boundaries of the 3 phase region.

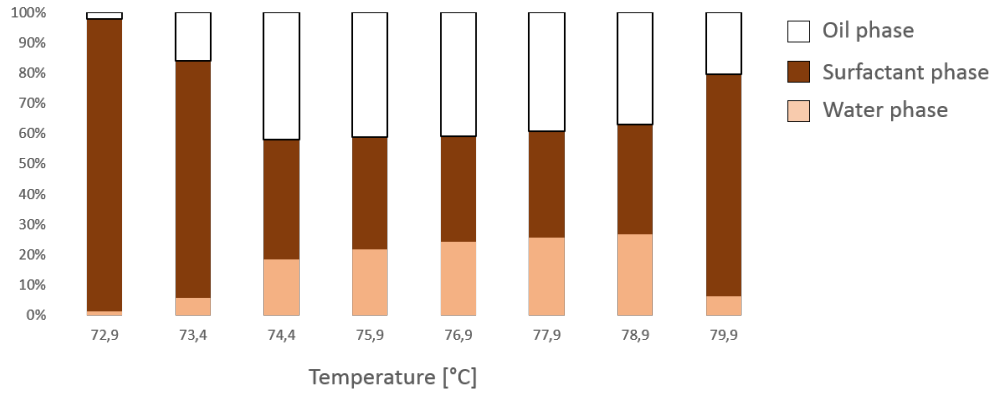


**Figure 4.8:** Phase separation state for different temperatures at concentrations  $\alpha = 0.5$ ,  $\gamma = 0.080$  and  $X = 0$

The experimental values of the relative level of the oil phase  $\varphi_{oil}$  as function of temperature  $T$  can be seen in Figure 4.9. As shown in the plot in red, a polynomial of order two was tested to fit the experimental data. Nevertheless, some points (marked with a green circle) that belong to the three phase region are not being covered by the fitted curve, and points that belong to the boundaries (small  $\varphi_{oil}$  value) are fitted correctly. This result is undesirable since the model would represent better the data in the boundaries and not in the most important separation regime.

A different approach was followed to benefit completely from the three phase data, that is, the data points between 74.5 and 79 °C. First, a two degree polynomial  $\varphi_{oil_{3ph}}$  curve was found exclusively for the three phase data (see Figure 4.10). Subsequently, sigmoidal trigger functions were used to establish the boundaries. The low temperature boundary is found between 73.4 and 74.4 °C, and the high temperature boundary is found between 78.9 and 79.9 °C, so the averages of these values are considered as the boundaries. The sigmoidal trigger functions used for these values are:

$$Trigger_{low} = \frac{1}{1 + e^{a(T-T_l)}} \quad (4.13)$$

$$Trigger_{high} = \frac{1}{1 + e^{-a(T-T_h)}} \quad (4.14)$$



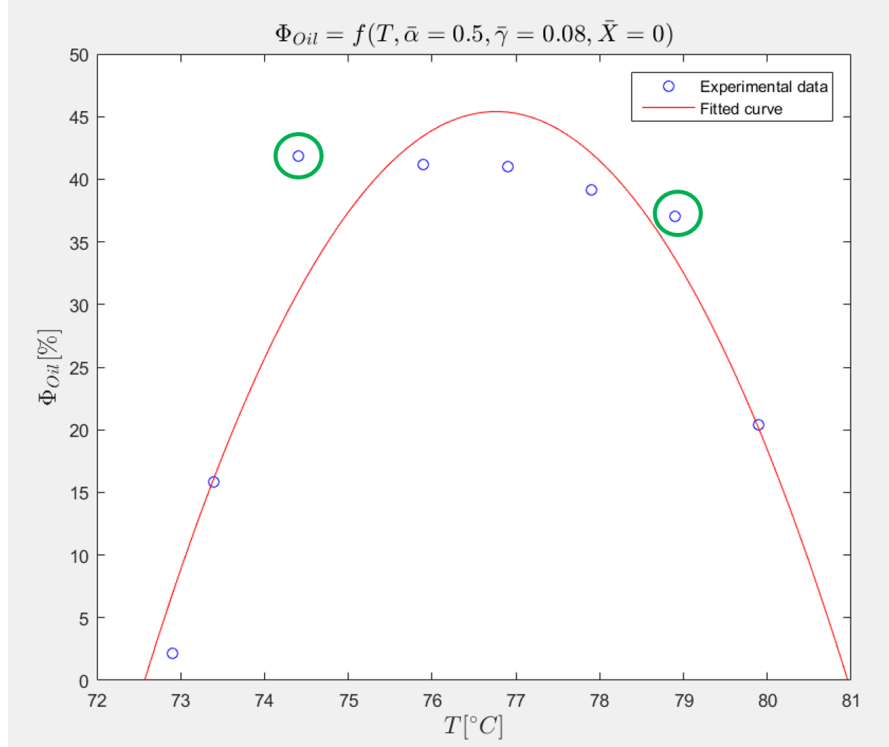


**Figure 4.9:** Experimental and model comparison for the relative level oil phase as a function of temperature. Concentrations  $\alpha = 0.5$ ,  $\gamma = 0.080$  and  $X = 0$

where  $a$  is the slope or steepness of the sigmoidal curve,  $T$  is the actual temperature of the mixture and,  $T_l$  and  $T_h$  are the temperature boundaries, which are:  $T_l = 73.9$  °C,  $T_h = 79.4$  °C.

The resultant function  $\hat{\varphi}_{oil}$  that fits the three phase data is finally structured as follows:

$$\hat{\varphi}_{oil} = \varphi_{oil_{3ph}} \cdot Trigger_{low} \cdot Trigger_{high} \quad (4.15)$$

The result obtained for this single experiment with the trigger function approach is depicted in Figure 4.11, where different values of slope  $a$  are used and compared. As described in Subsection 2.3, the steepness of the sigmoidal function of the trigger must be well selected to avoid non differentiabilitys. An appropriate result was found with steepness  $a = 50$  since the other values of slopes barely fits all of the three phase data.

A similar method was used for the relative level of water phase and the results are shown in Figure 4.12.

It is important to highlight that the values of the relative level of oil phase and water phase that are near the boundaries are not very well fitted by the curve (marked in green circle in respective pictures). Since it is of interest to operate the settler in the three phase region, this lack of accuracy around the boundaries can be permitted.

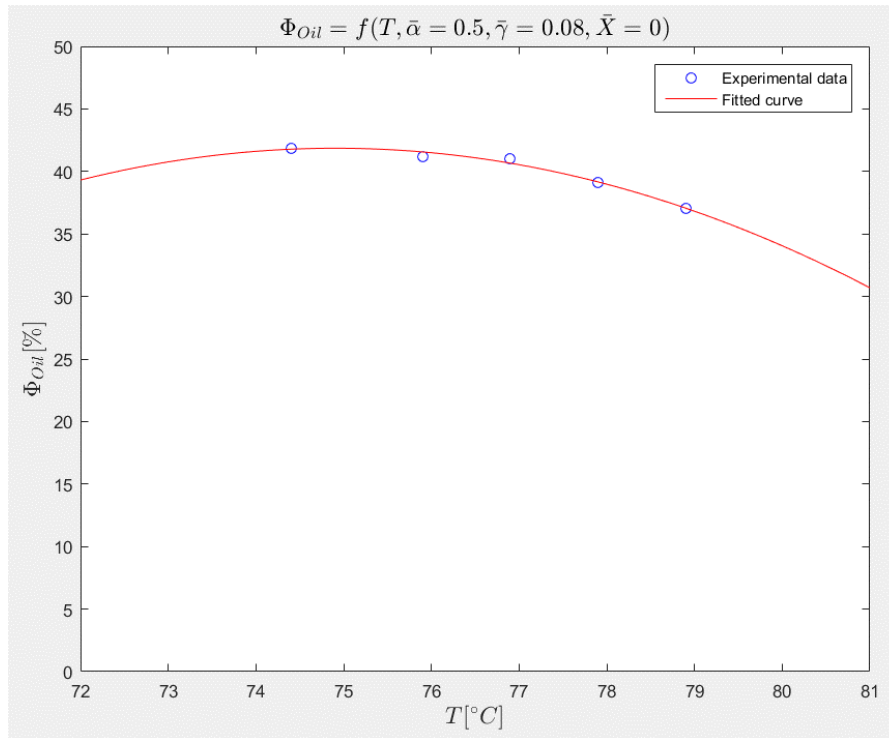


Figure 4.10: Polynomial fitting of order two for the three phase data at concentrations  $\alpha = 0.5$ ,  $\gamma = 0.080$  and  $X = 0$

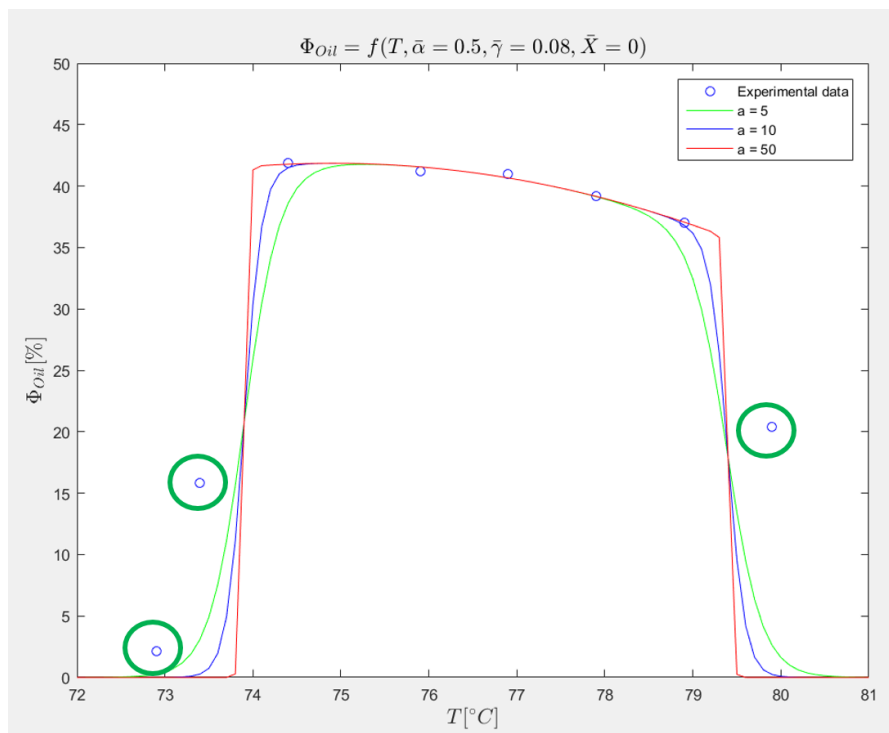
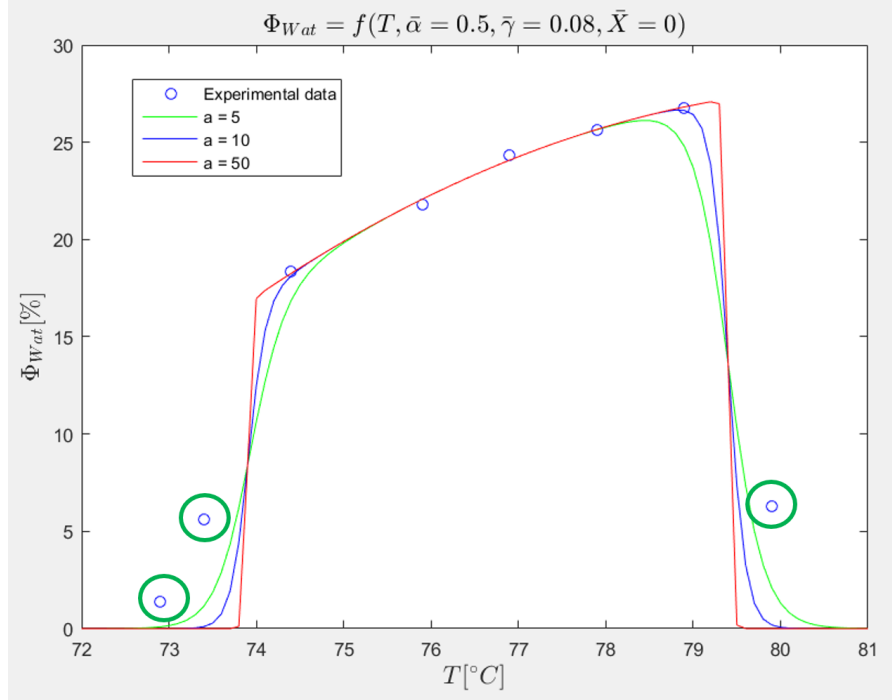


Figure 4.11: Fitted curve of oil phase using sigmoidal trigger functions with different slopes:  $a = 5$ ,  $a = 10$  and  $a = 50$ . Concentrations  $\alpha = 0.5$ ,  $\gamma = 0.080$  and  $X = 0$



**Figure 4.12:** Fitted curve of water phase using sigmoidal trigger functions with different slopes:  $a = 5$ ,  $a = 10$  and  $a = 50$ . Concentrations  $\alpha = 0.5$ ,  $\gamma = 0.080$  and  $X = 0$

### 4.5.2 Temperature boundaries vs. components concentration

As mentioned in the previous subsection, the temperature boundaries are key to define the operating window of the three phase region. Therefore, it is important to analyze how the temperature boundaries vary as a function of the component concentrations  $\alpha$ ,  $\gamma$  and  $X$ .

Figure 4.13 shows the experimental data that relate the temperature boundaries of the three phase region and surfactant, for a constant concentration of  $\bar{\alpha} = 0.5$  and  $\bar{X} = 0$ . In other words, this result is a small section of the Kahlweit's fish diagram.

Analyzing the trend of the experimental data it is concluded that a polynomial curve of order 2 can describe the relationship between the temperature and the surfactant for these specific component concentrations. A different behavior can be noticed for  $\bar{\alpha} = 0.5$  and  $\bar{X} = 0.4$ , shown in figure 4.14, where a polynomial of order two also fits, but the concavity of the function for the upper boundary is different compared to the one with  $\bar{X} = 0$ .

It is clear that the temperature boundaries of the three phase region are indeed affected by the concentrations of all three components. This means that the argument of the sigmoid functions (i.e.  $T_l$ ,  $T_h$ ), is in fact a multivariate function that depends on  $\alpha$ ,  $\gamma$  and  $X$ . Thus, the equation for the sigmoid functions are

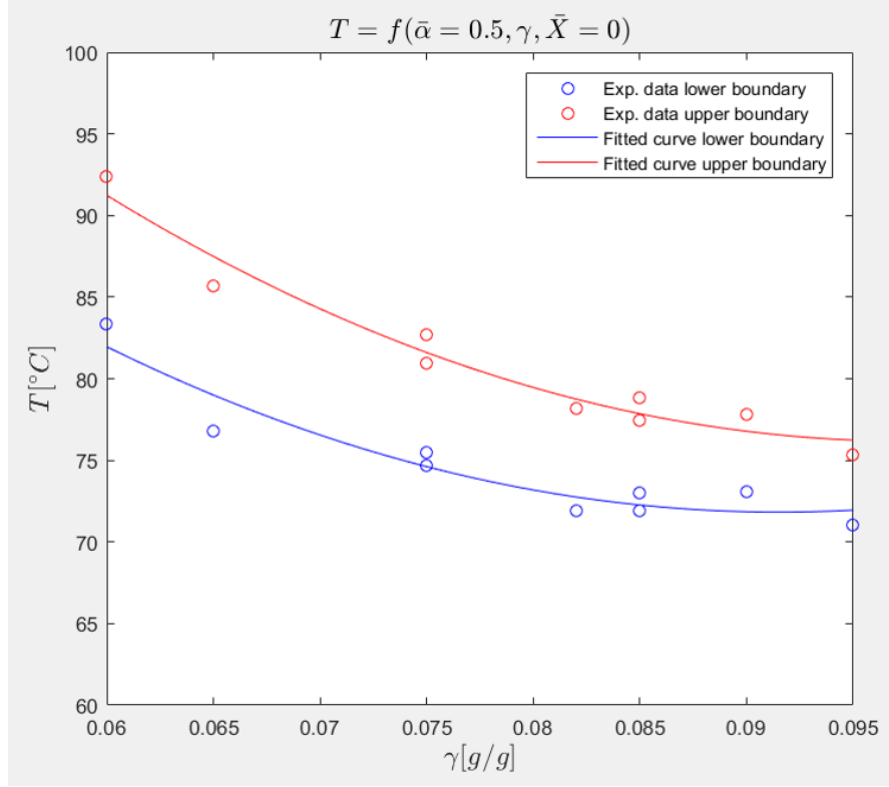


**Figure 4.13:** Temperature boundaries vs. Surfactant concentration for  $\bar{\alpha} = 0.5$  and  $\bar{X} = 0$ . Experimental data and fitted curve.

structured as follows:

$$Trigger_{low} = \frac{1}{1 + e^{50(T - T_l(\alpha, \gamma, X))}} \quad (4.16)$$

$$Trigger_{high} = \frac{1}{1 + e^{-50(T - T_h(\alpha, \gamma, X))}} \quad (4.17)$$

Where  $T_l$  and  $T_h$  are the lower and upper temperature boundaries of the three phase region, and they are a function of the component concentrations.

Therefore, before defining the model that describes the relative level of the phases as function of the concentrations and temperature, the temperature boundaries must be modeled first as function of  $\alpha$ ,  $\gamma$  and  $X$ .

## 4.6 Model family selection

The preliminary analysis of the data showed that the relationships between only two variables, such as the case of  $\varphi_{oil}$  - temperature and temperature -  $\gamma$  (seen in Section 4.5), can be explained with a quadratic function. This suggest, that for the multivariable case (four variables), an appropriate model family is again a polynomial regression.

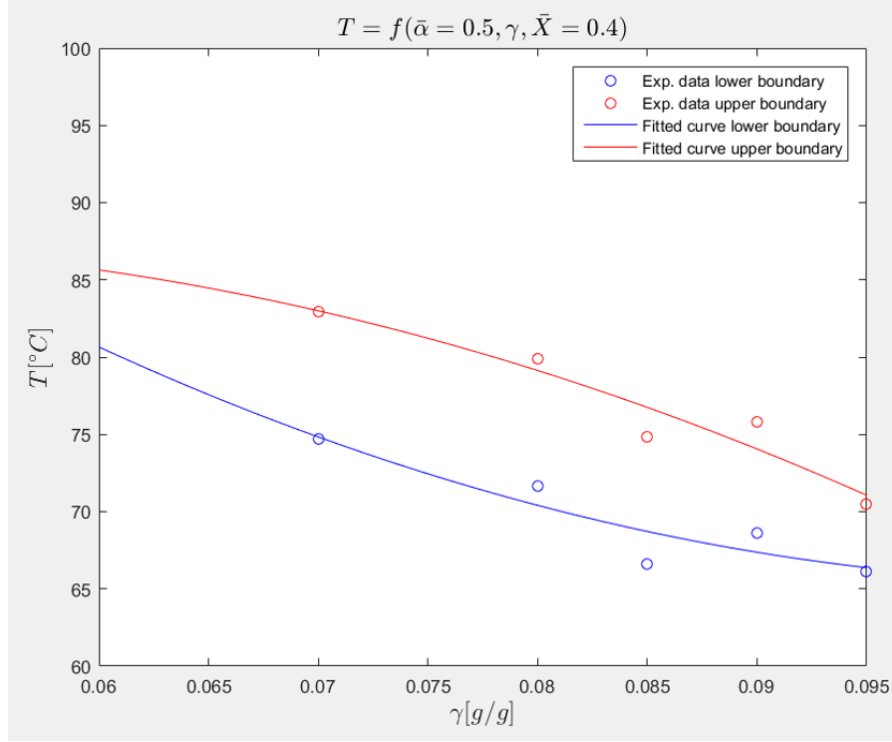


**Figure 4.14:** Temperature boundaries vs. Surfactant concentration for  $\bar{\alpha} = 0.5$  and  $\bar{X} = 0.4$ . Experimental data and fitted curve.

A block diagram containing the model structure is shown in picture 4.15. The parameters of the polynomial functions  $g_1(\alpha, \gamma, X)$  and  $g_2(\alpha, \gamma, X)$  are found based on the experimental data of the temperature boundaries. The functions  $f_1(T, \alpha, \gamma, X)$  and  $f_2(T, \alpha, \gamma, X)$  are parametrized according to experimental data of the 3 phase region ( $\varphi_{oil_{3ph}}$  and  $\varphi_{wat_{3ph}}$ ). Finally, with those curves, the estimated values of the relative levels  $\hat{\varphi}_{oil}$  and  $\hat{\varphi}_{wat}$  can be obtained.

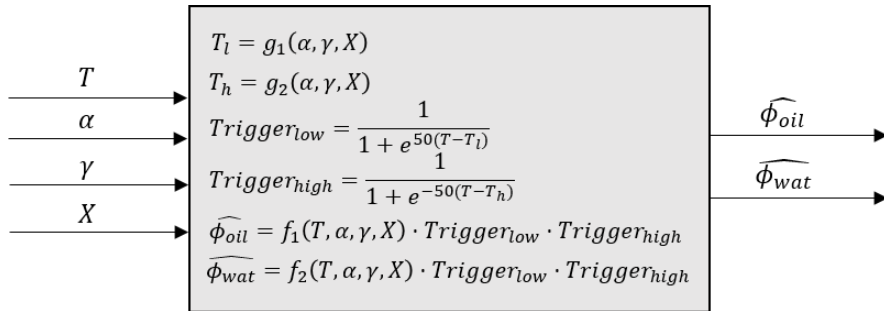


**Figure 4.15:** General model for the three phase separation state

## 4.7 Parameter estimation

To understand the estimation of the parameters of the polynomial functions  $g_1, g_2, f_1$  and  $f_2$ , a short review about polynomial regression is made in the following subsections.

### 4.7.1 Polynomial regression

The general equation of the polynomial model with one independent variable is:

$$y = \beta_0 + \beta_1x + \beta_2x^2 + \beta_3x^3 + \dots + \beta_kx^k + \varepsilon \quad (4.18)$$

where  $y$  is the measurable quantity or observed value,  $\beta_i$  are the parameters of the model,  $x$  is the regressor and  $\varepsilon$  is the error component (Sinha, 2013).

The equation can be expressed in matrix form as:

$$Y = \mathbf{X}\beta + \varepsilon \quad (4.19)$$

where  $Y$  is a vector of  $n$  observations,  $\mathbf{X}$  is an  $n \times k$ -vector of known quantities also called *regression variables* or *regressors*, and  $\beta$  is an  $n$ -vector of unknown parameters.

Even though the polynomial model is nonlinear, the regression function is linear in the parameters. Hence, the values of the unknown  $\beta$  are estimated through the Least Squares (LS) method.

The LS method consists in finding the estimation  $\hat{\beta}$  that minimizes the sum of prediction errors.

Assuming that the fitted regression equation is:

$$\hat{y} = \hat{\beta}_0 + \hat{\beta}_1x + \hat{\beta}_2x^2 + \hat{\beta}_3x^3 + \dots + \hat{\beta}_kx^k \quad (4.20)$$

Then by LS method, the minimum error is represented as:

$$SSE = \sum_{i=1}^n (y_i - \hat{\beta}_0 + \hat{\beta}_1x + \hat{\beta}_2x^2 + \hat{\beta}_3x^3 + \dots + \hat{\beta}_kx^k) \quad (4.21)$$

Which can be written in matrix representation as:

$$SSE = Y^T Y - 2\hat{\beta}\mathbf{X}^T Y^T + \hat{\beta}\mathbf{X}^T \mathbf{X} \hat{\beta} \quad (4.22)$$

By partial differentiation with respect to the regression equation model parameters, the values of the parameters can be found as:

$$\hat{\beta} = (\mathbf{X}^T \mathbf{X})^{-1} \mathbf{X}^T Y \quad (4.23)$$

To evaluate the accuracy of the fit or, in other words, how well the regression curve fits the data, the coefficient of determination  $R_2$  can be used. This coefficient provides a measure of how the total variation of the dependent variable is explained by the regression model (Gujarati and Porter, 2009). Its limits are  $0 \leq R_2 \leq 1$ , where zero means that there is no relationship between the independent value and the regressors, and the value of one means perfect fit. The  $R_2$  value can be calculated as follows:

$$R^2 = 1 - \frac{SSE}{SST} \quad (4.24)$$

where  $SSE = \sum_i^n (y_i - \hat{y}_i)^2$  is the sum of the squares of residuals and  $SST = \sum_i^n (y_i - \bar{y}_i)^2$  is the total sums of squares. For example, an  $R_2$  of 0.8 means that the 80 % of the points fall within the regression curve.

The  $R_2$  value will always increase approaching to 1 when the order of the model increases. This means that more complex regression models tend to fit better the data. But, not necessarily increasing the  $R_2$  value means that the model is better. In practice, a high value of  $R_2$  does not always imply the best choice of parameters or model order. Higher order models tend to fit also noise, this is known as overfitting and it is undesirable.

The MATLAB<sup>®</sup> function *polyfitn*, developed by John D'Errico, was used to estimate the parameters of the multivariable polynomial curves  $g_1, g_2, f_1$  and  $f_2$ . This function uses QR factorization, to solve the linear least squares problem. The function *polyfitn* gives also information about the  $R_2$  and MSE values which are useful to assess the accuracy of the fit.

The parameters of different model structures were found using *polyfitn*, but since a high  $R^2$  value does not always represent a better model for the data, since overfitting may occur, the cross validation method was performed to select the appropriate model structure.

## 4.8 Model Validation

### 4.8.1 Basic concept

Once a model structure and its parameters are estimated, the following procedure for system identification is to assess or validate it. Models reproduce the estimation data very well when the inputs belong to the training set of data. Therefore, it is necessary to use another set of data, that has not been used for the training process. This is known as test or validation process.

*Cross-validation* is a technique in which the available set of  $n$  observations is divided randomly into two parts, a training set and a validation or testing set. The training set is used for the construction of the model and the testing set is used for the model validation. The validation error is typically assessed using the *Mean Squared Error* or *MSE*, which is defined as follows:

$$MSE = \frac{1}{n} \sum_{i=1}^n (\hat{y}_i - y_i)^2 \quad (4.25)$$

The MSE value is calculated for  $n$  randomly chosen partitions and evaluated for different model orders. There are two methods in which the sets of data can

be splitted into training and testing set (James et al., 2014): *Leave one-out cross-validation* and *K-fold cross-validation*. This section will be limited only to the discussion of the LOOCV method.

### Leave One-Out Cross-Validation (LOOCV)

This cross-validation method involves splitting the set of  $n$  observations into two sets: A testing set which is composed of one single observation, and the remaining observations are used for the training process. This technique is performed repeatedly  $n - 1$  times, making sure that every observation is used for testing one time. A schematic display of this method is shown in figure 4.16.

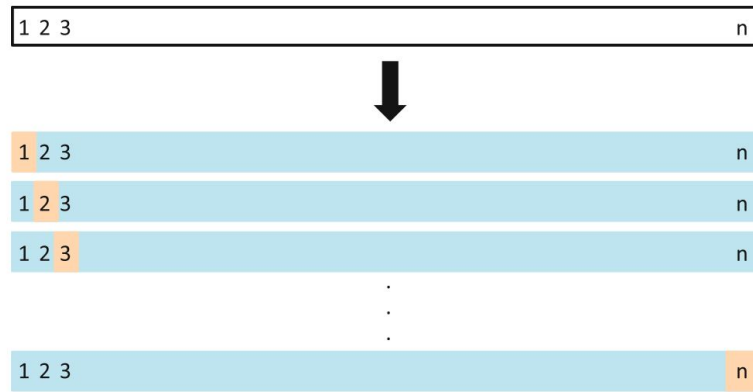


**Figure 4.16:** Schematic of LOOCV partitions. Image taken from James et al., 2014

The  $MSE$  is then calculated for each partition and the LOOCV estimate is the average of these  $n$  test error estimates:

$$CV_{(n)} = \frac{1}{n} \sum_{i=1}^n MSE_i \tag{4.26}$$

Since the validation method has to be performed  $n$  times and for every model structure, the LOOCV is computational expensive to implement. Specially if  $n$  is large and if each individual model is slow to fit.

### 4.8.2 Selection of the suitable model for phase separation

The set of experimental data is small, so the Leave One-Out Cross-Validation method explained in subsection 4.8.1 is used. This method was performed to find the suitable structures of the functions  $f_1, f_2, g_1$  and  $g_2$ . The results are discussed in the following sections.

#### Temperature boundaries models

Different polynomial functions were validated to find the best solution for  $g_1(\alpha, \gamma, X)$  and  $g_2(\alpha, \gamma, X)$ . These models are:



- Model 1: Polynomial of order 1

$$T_l = \beta_0 + \beta_1 \cdot \alpha + \beta_2 \cdot \gamma + \beta_3 \cdot X \quad (4.27)$$

- Model 2: Polynomial of order 2

$$T_l = \beta_0 + \beta_1 \cdot \alpha + \beta_2 \cdot \gamma + \beta_3 \cdot X + \beta_4 \cdot \alpha^2 + \beta_5 \cdot \gamma^2 + \beta_6 \cdot X^2 \quad (4.28)$$

- Model 3:

$$T_l = \beta_0 + \beta_1 \cdot \alpha + \beta_2 \cdot \gamma + \beta_3 \cdot X + \beta_4 \cdot \alpha \cdot \gamma + \beta_5 \cdot \gamma \cdot X + \beta_6 \cdot \alpha \cdot X + \beta_7 \cdot \alpha^2 + \beta_8 \cdot \gamma^2 + \beta_9 \cdot X^2 \quad (4.29)$$

- Model 4:

$$T_l = \beta_0 + \beta_1 \cdot \alpha + \beta_2 \cdot \gamma + \beta_3 \cdot X + \beta_4 \cdot \alpha \cdot \gamma + \beta_5 \cdot \gamma \cdot X + \beta_6 \cdot \alpha \cdot X + \beta_7 \cdot \alpha \cdot \gamma \cdot X + \beta_8 \cdot \alpha^2 + \beta_9 \cdot \gamma^2 + \beta_{10} \cdot X^2 \quad (4.30)$$

- Model 5:

$$T_l = \beta_0 + \beta_1 \cdot \alpha + \beta_2 \cdot \gamma + \beta_3 \cdot X + \beta_4 \cdot \alpha^2 + \beta_5 \cdot \gamma^2 + \beta_6 \cdot X^2 + \beta_7 \cdot \alpha^3 + \beta_8 \cdot \gamma^3 + \beta_9 \cdot X^3 \quad (4.31)$$

The same model structures were validated for the lower and upper temperature boundary. Figures 4.17a and 4.17b show the R2 and Mean Squared Error MSE obtained in training and testing of the lower temperature boundary models.

As seen in the pictures, the model with smaller MSE value and with a relative small increase between the training and testing set of data is Model 2. This model structure has a large value of  $R^2 = 0.8838$ . Even though this model does not have the biggest coefficient of determination, the MSE values confirm that is the best model that represents the lower temperature boundary data as function of the components concentrations.

Figures 4.18a and 4.18b show the R2 and Mean Squared Error MSE obtained in training and testing of the upper temperature boundary models.

As seen in the pictures, the model with smaller MSE value and with a relative small increase between the training and testing set of data is Model 2. This model structure has a value of  $R^2 = 0.7969$ . Even though this model does not have the biggest coefficient of determination, the MSE values confirm that is the best model

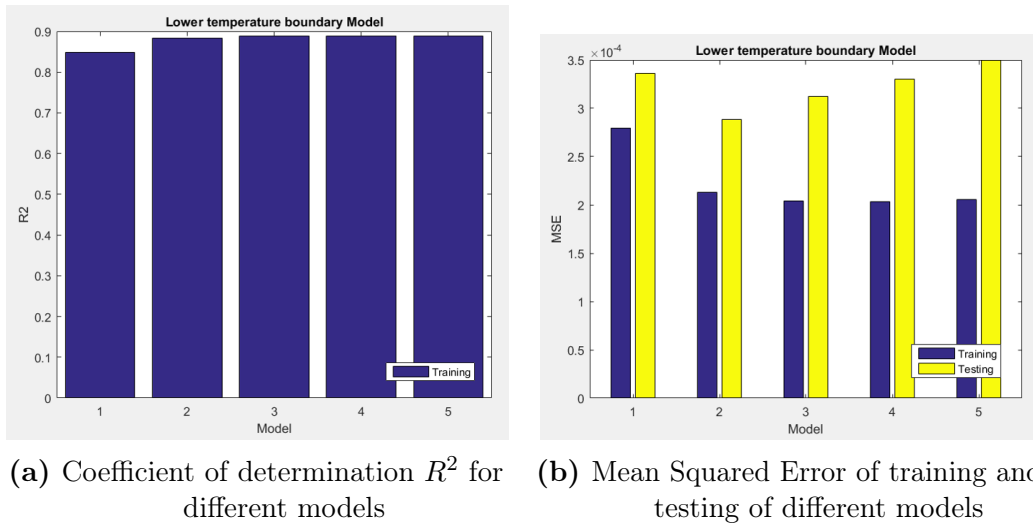


**Figure 4.17:** Comparison of MSE and  $R^2$  values for different model structures of the lower temperature boundary

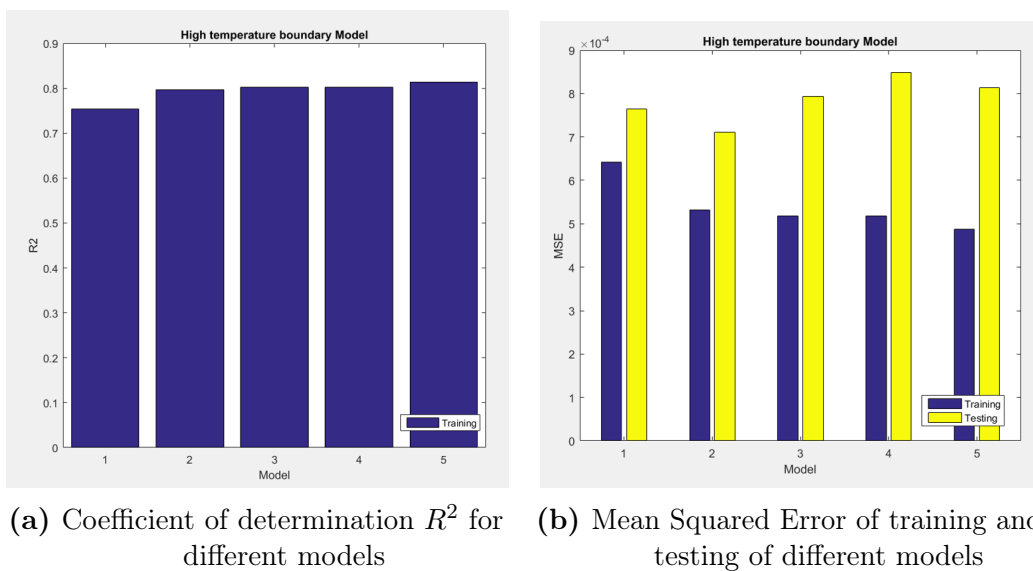


**Figure 4.18:** Comparison of MSE and  $R^2$  values for different model structures of the upper temperature boundary

that represents the lower temperature boundary data as function of the components concentrations.

On the other hand, Figure 4.19, shows a comparison of the estimated values of the temperature boundaries with the selected model and the experimental data of variable compositions  $\gamma$  and  $X$ , and a constant composition of  $\alpha = 0.5$ .

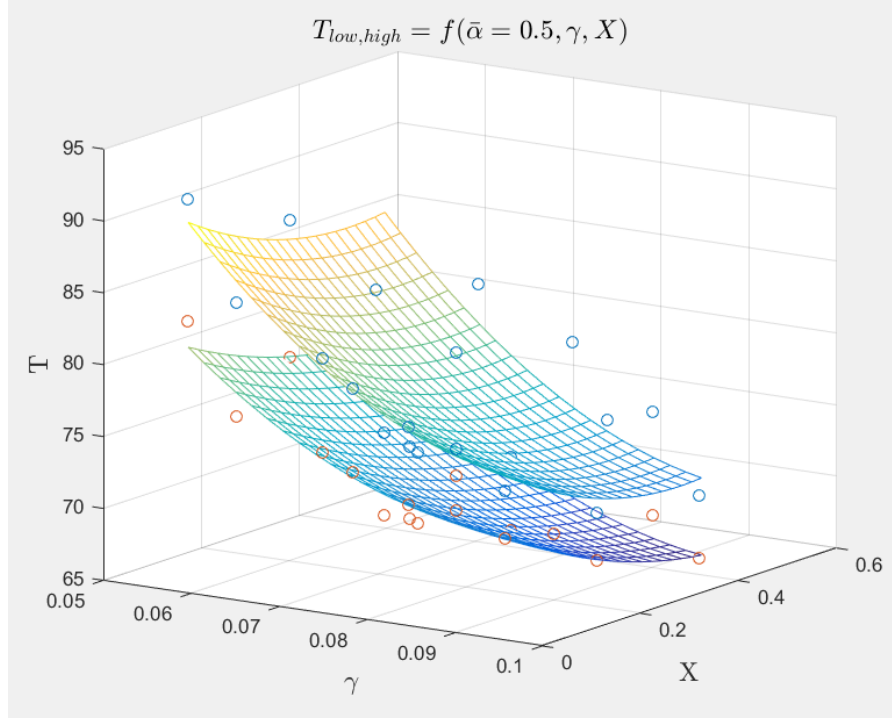


**Figure 4.19:** Temperature boundaries fitted surfaces for the experimental data. Constant concentration  $\alpha = 0.5$  and variable concentrations  $\gamma$  and  $X$ .

### Relative level of oil and water phase models

Different polynomial functions were validated to find the best solution for  $f_1(T, \alpha, \gamma, X)$  and  $f_2(T, \alpha, \gamma, X)$ . The models are:

- Model 1:

$$\varphi_{3ph} = \beta_0 + \beta_1 \cdot T + \beta_2 \cdot \alpha + \beta_3 \cdot \gamma + \beta_4 \cdot X \quad (4.32)$$

- Model 2:

$$\varphi_{3ph} = \beta_0 + \beta_1 \cdot T + \beta_2 \cdot \alpha + \beta_3 \cdot \gamma + \beta_4 \cdot X + \beta_5 \cdot T^2 + \beta_6 \cdot \alpha^2 + \beta_7 \cdot \gamma^2 + \beta_8 \cdot X^2 \quad (4.33)$$

- Model 3:

$$\begin{aligned} \varphi_{3ph} = & \beta_0 + \beta_1 \cdot T + \beta_2 \cdot \alpha + \beta_3 \cdot \gamma + \beta_4 \cdot X \\ & + \beta_5 \cdot T \cdot \alpha + \beta_6 \cdot \alpha \cdot \gamma + \beta_7 \cdot \gamma \cdot X + \beta_8 \cdot T \cdot \gamma + \beta_9 \cdot \alpha \cdot X \\ & + \beta_{10} \cdot T^2 + \beta_{11} \cdot \alpha^2 + \beta_{12} \cdot \gamma^2 + \beta_{13} \cdot X^2 \end{aligned} \quad (4.34)$$

- Model 4:

$$\begin{aligned}\varphi_{3ph} = & \beta_0 + \beta_1 \cdot T + \beta_2 \cdot \alpha + \beta_3 \cdot \gamma + \beta_4 \cdot X \\ & + \beta_5 \cdot T \cdot \alpha + \beta_6 \cdot \alpha \cdot \gamma + \beta_7 \cdot \gamma \cdot X + \beta_8 \cdot T \cdot \gamma + \beta_9 \cdot \alpha \cdot X \\ & + \beta_{10} \cdot T \cdot X + \beta_{11} \cdot T \cdot \alpha \cdot \gamma + \beta_{12} \cdot \alpha \cdot \gamma \cdot X + \beta_{13} \cdot T \cdot \alpha \cdot \gamma \cdot X \\ & + \beta_{14} \cdot T^2 + \beta_{15} \cdot \alpha^2 + \beta_{16} \cdot \gamma^2 + \beta_{17} \cdot X^2\end{aligned}\quad (4.35)$$

- Model 5:

$$\begin{aligned}\varphi_{3ph} = & \beta_0 + \beta_1 \cdot T + \beta_2 \cdot \alpha + \beta_3 \cdot \gamma + \beta_4 \cdot X \\ & + \beta_5 \cdot T \cdot \alpha + \beta_6 \cdot \alpha \cdot \gamma + \beta_7 \cdot \gamma \cdot X + \beta_8 \cdot T \cdot \gamma + \beta_9 \cdot \alpha \cdot X + \beta_{10} \cdot T \cdot X \\ & + \beta_{11} \cdot T \cdot \alpha \cdot \gamma + \beta_{12} \cdot \alpha \cdot \gamma \cdot X + \beta_{13} \cdot T \cdot \alpha \cdot \gamma \cdot X\end{aligned}\quad (4.36)$$

- Model 6:

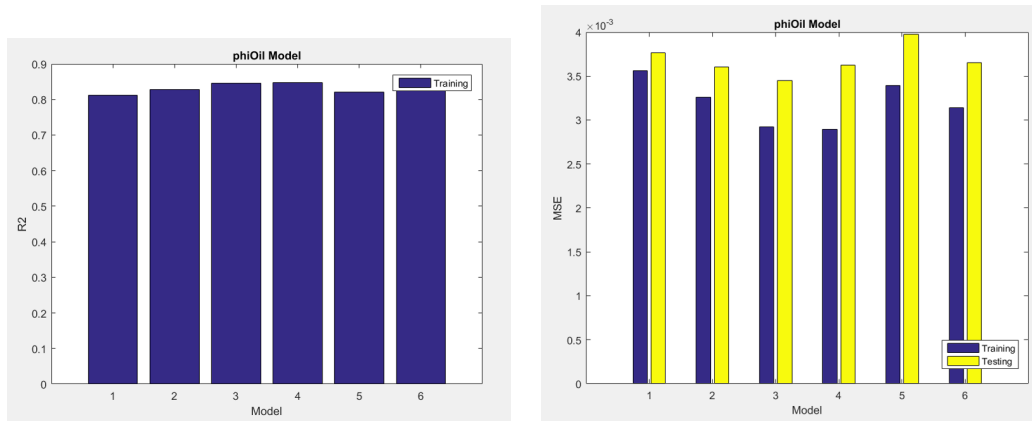
$$\begin{aligned}\varphi_{oil_{3ph}} = & \beta_0 + \beta_1 \cdot T + \beta_2 \cdot \alpha + \beta_3 \cdot \gamma + \beta_4 \cdot X + \beta_5 \cdot T^2 + \beta_6 \cdot \alpha^2 + \\ & \beta_7 \cdot \gamma^2 + \beta_8 \cdot X^2 + \beta_9 \cdot T^3 + \beta_{10} \cdot \alpha^3 + \beta_{11} \cdot \gamma^3 + \beta_{12} \cdot X^3\end{aligned}\quad (4.37)$$

The same model structures were validated for the relative level of oil and water phases. Figures 4.20a and 4.20b show the R2 and Mean Squared Error MSE obtained in training and testing of the relative level of oil phase in the three phase region. As seen in the images, the model with smaller MSE value and with a relative small increase between the training and testing set of data is the Model 3. This model structure has a value of  $R^2 = 0.8455$  which is the largest coefficient of determination among all.

Model 3 is the model that best represents the relative oil phase level as function of the temperature and components concentrations. Figure 4.21 presents a comparison of the estimated values of the relative level of oil phase with the selected model and the experimental data with variable compositions  $\gamma$  and  $T$ , and a constant composition of  $\alpha = 0.5$  and  $X = 0$ .

Additionally, Figures 4.22a and 4.22b show the R2 and Mean Squared Error MSE obtained in training and testing of the relative level of water phase in the three-phase region. Model structure 3, is the model with the smallest MSE value, with a relative small increase of MSE between the training and testing set of data, and it has a value of  $R^2 = 0.6807$ , which is the largest coefficient of determination among all.

Even though the  $R^2$  for the water volume fraction is low, it does not indicate that the model is not appropriate. This low value is due to the high sources of error in the measurements. Therefore, Model 3 is the model that best represents the relative water phase level as function of the temperature and components concentrations.



(a) Coefficient of determination  $R^2$  for different models (b) Mean Squared Error of training and testing of different models

**Figure 4.20:** Comparison of MSE and  $R^2$  values for different model structures of the relative level of oil phase

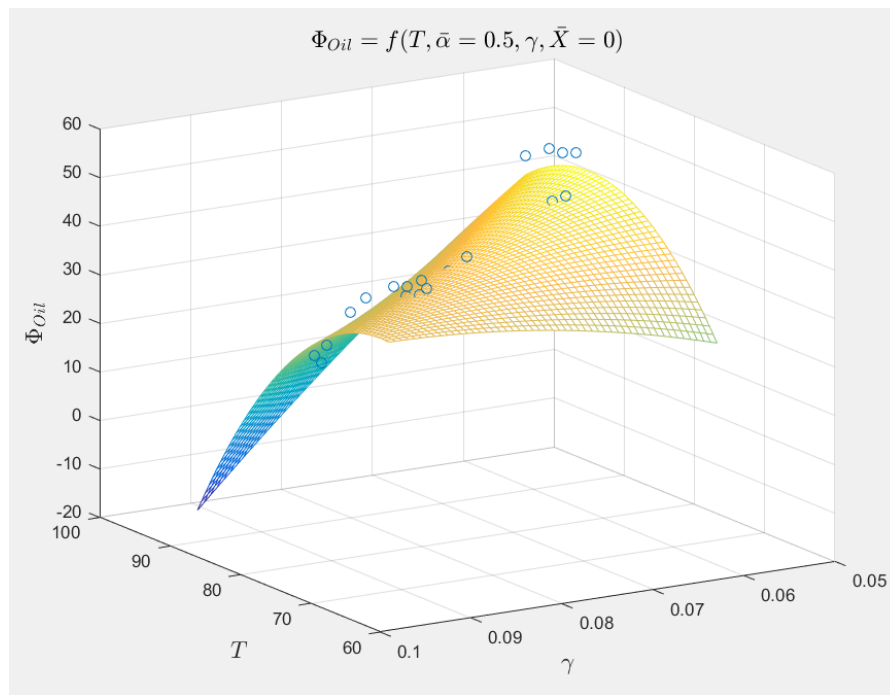
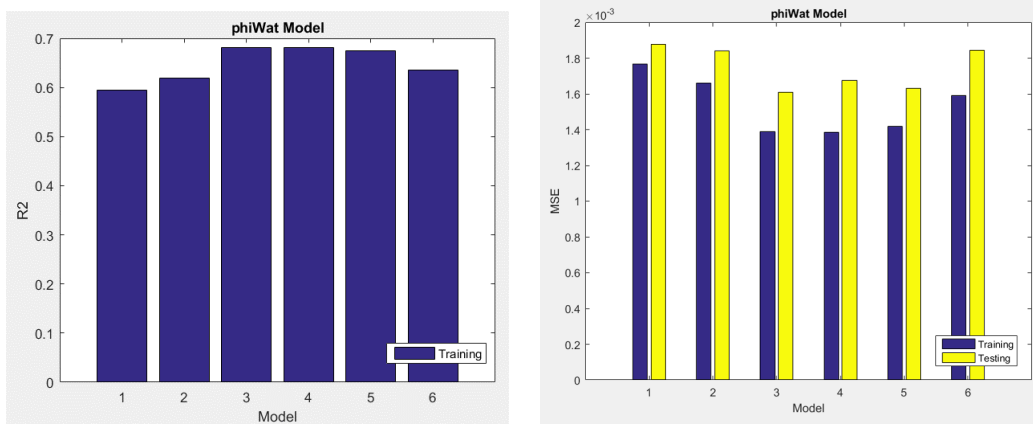


**Figure 4.21:** Fitted surface for relative level of oil phase at constant concentration  $\alpha = 0.5$  and  $X = 0$  and variable concentrations  $\gamma$  and  $T$ .

Figure 4.23 presents a comparison of the estimated values of the relative level of water phase with the selected model and the experimental data with variable compositions  $\gamma$  and  $T$ , and a constant composition of  $\alpha = 0.5$  and  $X = 0$ .

### Resultant Model of the three-phase separation behavior

Once all the suitable functions are selected, the description of the three phase separation of a microemulsion is represented by  $\hat{\varphi}_{oil}$  and  $\hat{\varphi}_{wat}$ . As discussed in



(a) Coefficient of determination  $R^2$  for different models (b) Mean Squared Error of training and testing of different models

**Figure 4.22:** Comparison of MSE and  $R^2$  values for different model structures of the relative level of water phase

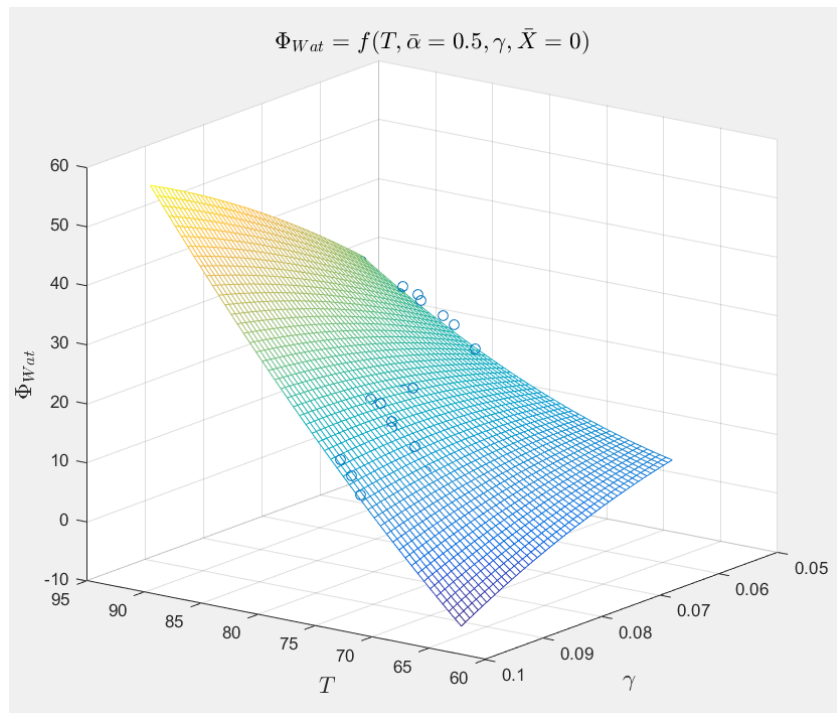


**Figure 4.23:** Fitted surface for relative level of water phase at constant concentration  $\alpha = 0.5$  and  $X = 0$  and variable concentrations  $\gamma$  and  $T$ .

subsection 4.6, the functions  $g_1$  and  $g_2$  are the arguments of the trigger functions that bound the three phase region, and functions  $f_1$  and  $f_2$  are the models of the phase levels in the three phase region. Integrating all those functions, the resultant model of  $\hat{\varphi}_{oil}$  and  $\hat{\varphi}_{wat}$  can be found.

A comparison of the estimated values of  $\hat{\varphi}_{oil}$  and the experimental data for constant concentrations  $\alpha = 0.5$  and  $X = 0$  and variable concentrations  $\gamma$  and  $T$

are shown in figure 4.24.

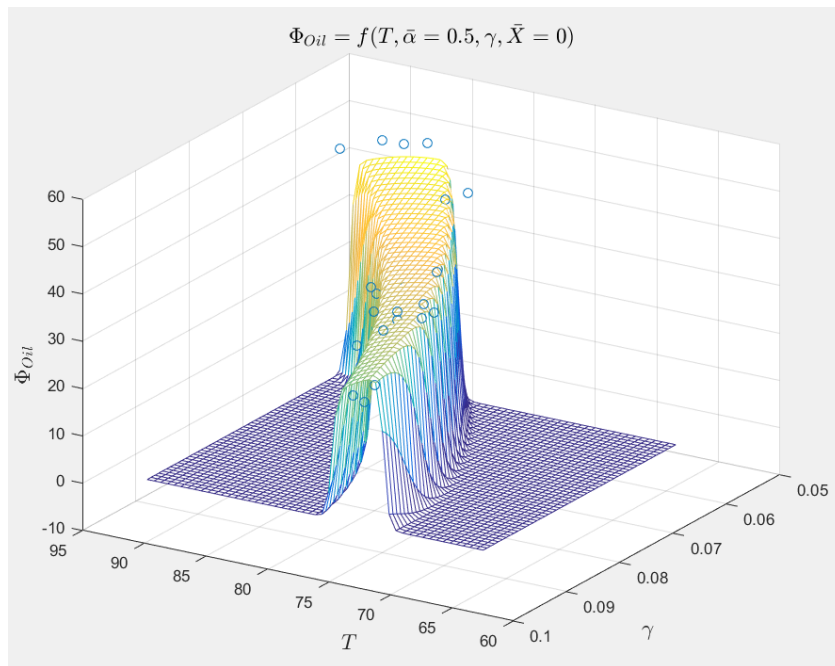


**Figure 4.24:** Fitted surface for relative level of oil phase at constant concentration  $\alpha = 0.5$  and  $X = 0$  and variable concentrations  $\gamma$  and  $T$ .

A similar comparison, shown in figure 4.25, is made for  $\hat{\varphi}_{wat}$ .

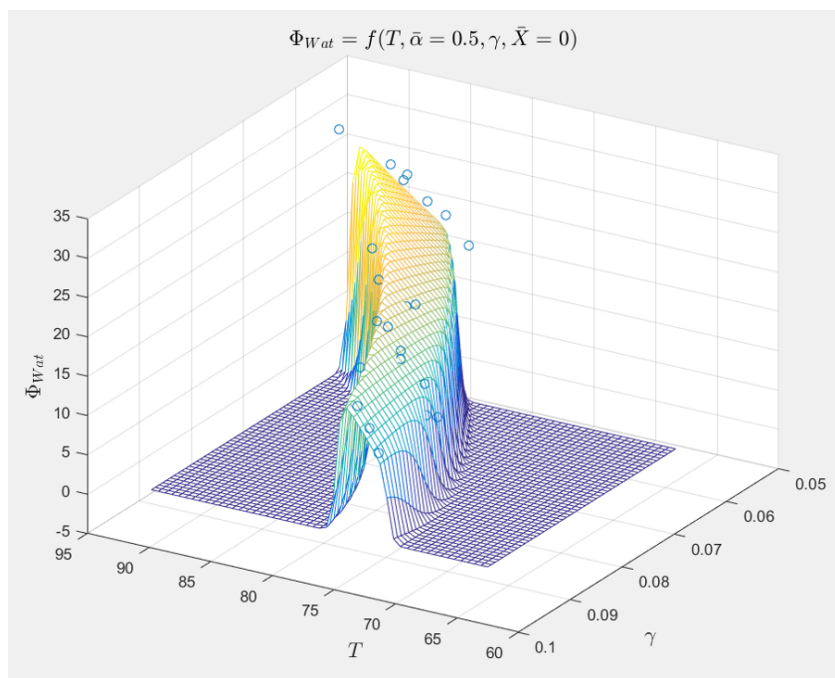


**Figure 4.25:** Fitted surface for relative level of water phase at constant concentration  $\alpha = 0.5$  and  $X = 0$  and variable concentrations  $\gamma$  and  $T$ .

These final models are used to create an operating region and to develop the soft-sensor of the surfactant concentration  $\gamma$  and oil to water ratio  $\alpha$ , which will be explained in Chapter 5.



# Chapter 5

## Integration in the Control System Siemens PCS7

The three-phase separation model described in Chapter 4 is used for three main purposes. The first, is to be used to complete the mini-plant model for the D-RTO framework. The second, is to plot an operating window for the three-phase region, which will be visualized in the control system. The third goal is to estimate the surfactant concentration and oil to water ratio from the plant measurements (temperature  $T$ , conversion  $X$ , and volume fractions  $\varphi_{oil}, \varphi_{wat}$ ). In the next sections the operating region and the soft-sensor developments are explained.

### 5.1 Operating Region plot

Only under certain process conditions the three-phase separation region can be achieved. A representation of this region can be obtained from the model, in which  $\varphi_{oil}$  and  $\varphi_{wat}$  are maximum in the three-phase region, and decrease considerably while reaching the boundaries.

The operator of the mini-plant must visualize in the Human-Machine Interface HMI, where the three phase region is located for a certain settler temperature and conversion, along the full operating range of  $\alpha : [0.4, 0.6]$  and  $\gamma : [0.06, 0.01]$ . An example can be shown in Figure 5.1, where the plot is the top view of the sum of  $\varphi_{oil}$  and  $\varphi_{wat}$  surfaces for a constant temperature and conversion. The sum of the volume fractions of the phases are maximum inside the three phase region (in yellow) and zero outside the three phase region (in blue). The operator can analyze under which concentrations of  $\alpha$  and  $\gamma$  the three phase region can be achieved, considering the actual temperature and conversion values inside the settler.

To plot this operating window are necessary the polynomials of the model developed in 4, and the process values: Temperature  $T$  and conversion  $X$ . Figure 5.2 illustrates through a block diagram, the inputs and the outputs path.

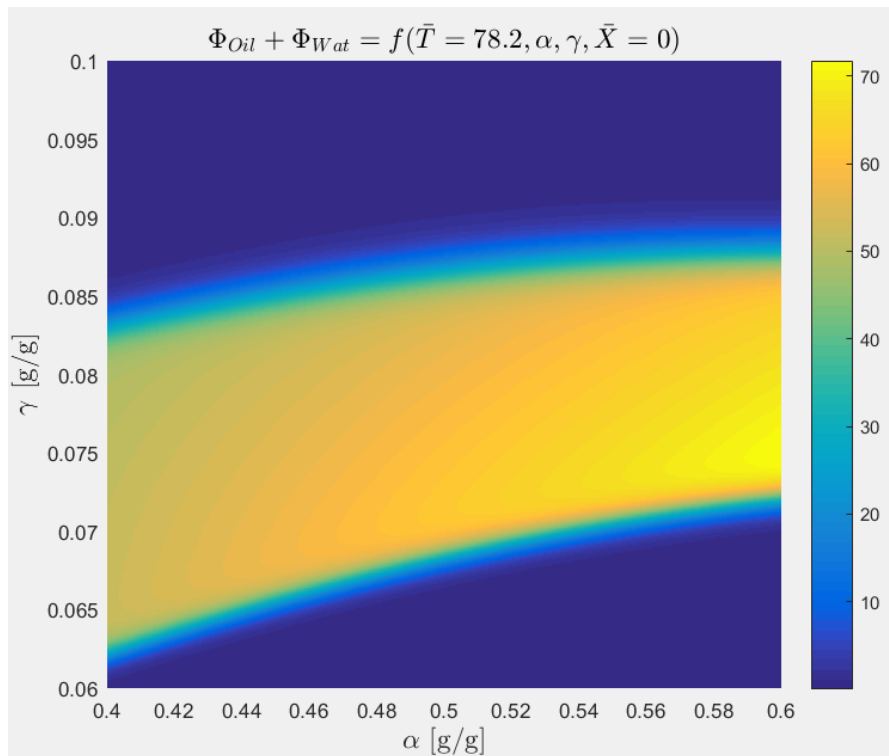


**Figure 5.1:** Operating region for a measured temperature of  $T = 78.2^\circ\text{C}$  and conversion  $X = 0$

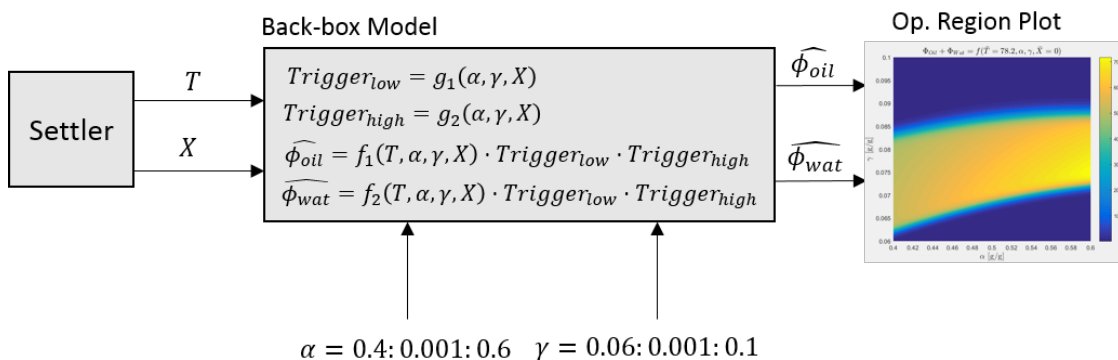


**Figure 5.2:** Block diagram for determination of the operating region plot at actual process conditions

## 5.2 Soft-sensor for surfactant concentration and oil to water ratio

The operator can visualize through the operating window plot the three phase region at certain process conditions. Additionally, the operator must have the knowledge about in which part of the three-phase region the settler is operating. This information can be achieved through the estimation of the surfactant concentration and the oil to water ratio. The overall structure for the soft-sensing of the surfactant concentration and the oil-to-water ratio, is shown in Figure 5.3

Since the developed model takes as inputs  $T$ ,  $\alpha$ ,  $\gamma$  and  $X$ , and the outputs are

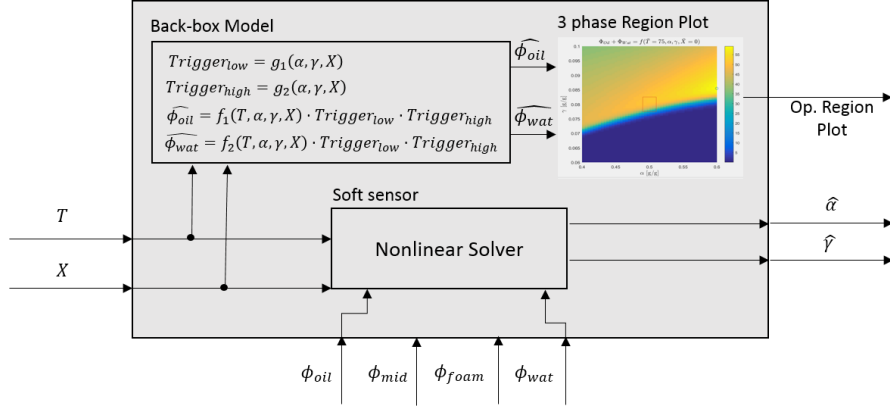


Figure 5.3: Soft-Sensor structure, inputs and outputs

$\varphi_{oil}$  and  $\varphi_{wat}$ , the system of equations shown in equation (5.1) need to be solved for  $\alpha$  and  $\gamma$ . The values of the inputs  $T$ ,  $X$ ,  $\varphi_{oil}$ ,  $\varphi_{wat}$  are provided by the field measurements and the image processing algorithm.

$$\begin{cases} \varphi_{oil} = f_1(T, \alpha, \gamma, X) \cdot \left( \frac{1}{1+e^{50(T-g_1(\alpha, \gamma, X))}} \right) \cdot \left( \frac{1}{1+e^{-50(T-g_2(\alpha, \gamma, X))}} \right) \\ \varphi_{wat} = f_2(T, \alpha, \gamma, X) \cdot \left( \frac{1}{1+e^{50(T-g_1(\alpha, \gamma, X))}} \right) \cdot \left( \frac{1}{1+e^{-50(T-g_2(\alpha, \gamma, X))}} \right) \end{cases} \quad (5.1)$$

Nonlinear least squares is used in MATLAB<sup>®</sup> to solve the equation system for  $\alpha$  and  $\gamma$ . The constraints are  $0.4 \leq \alpha \leq 0.6$  and  $0.06 \leq \gamma \leq 0.1$ , which the minimum and maximum values lie in the operating conditions at subsection 2.2.4.

The estimation  $\hat{\alpha}$  and  $\hat{\gamma}$  is included in the operating region plot (blue dot), as shown in figure 5.4. Besides, a red rectangle depicted inside the plot represents the set-point for  $\alpha$  and  $\gamma$  calculated with the optimizer. The task of the operator is to take actions in the mini-plant, for example, change the recycle ratios of the pumps or add more surfactant, etc., to lead the separation state to the optimal set-point.

## 5.3 Communication architecture

The image processing algorithm runs in a computer located outside the mini-plant (see Figure 5.5). The program is in charge of capturing the webcam images and analyzing them for level detection. The information about the volume fractions of the phases and the processed picture are stored in the OS-Server. The operator uses the SCADA system to insert the lower and upper boundaries of the setpoints of  $\alpha$  and  $\gamma$ . The MATLAB program, which holds the soft-sensor and creates the operating region plot, reads the field process values  $T$  and  $X$  and the concentration setpoints through OPC communication. Afterwards, the values of  $\alpha$  and  $\gamma$  are estimated, and the operating region plot is created. These results are sent and

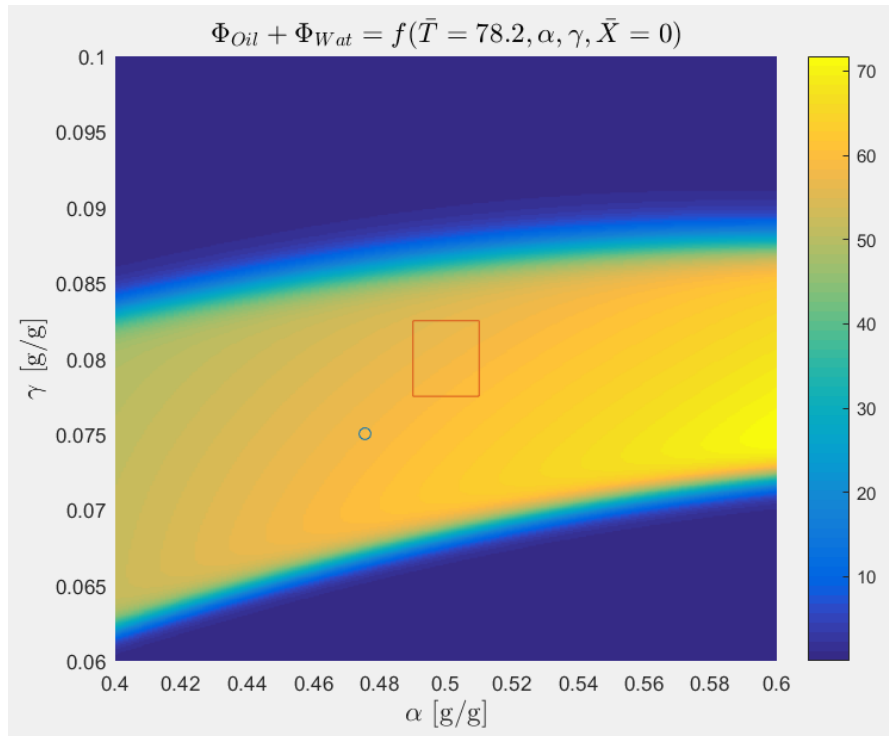


**Figure 5.4:** Operating region plot with estimated values of  $\alpha$  and  $\gamma$  (blue dot) and set-point (red rectangle)

visualized in the SCADA system.

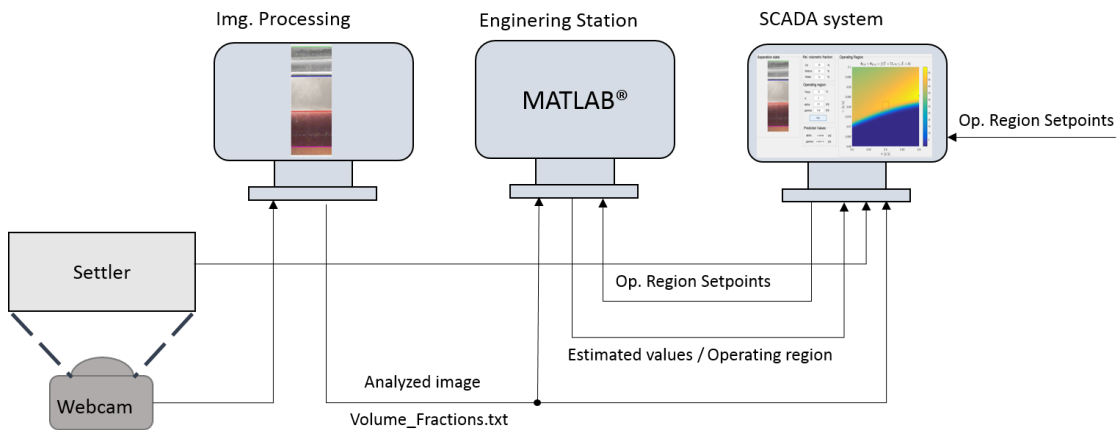


**Figure 5.5:** Scheme of communication for the automatic solution

## 5.4 Visualization in Siemens PCS7

Finally, the soft-sensor and the image processing outputs are integrated to the SCADA system. Figure 5.6 depicts the designed visualization interface of the soft-sensor and the processed image. The process values temperature  $T$ , conversion

$Y$ , and volumetric fractions  $\varphi_{oil}$ ,  $\varphi_{foam}$ ,  $\varphi_{surf}$ ,  $\varphi_{wat}$  are visualized in the main panel of the settler. When the operator clicks the button "Soft-sensor" another panel is opened showing the operating region plot and the estimated values of the concentrations for the actual separation state. The operator can insert the upper and lower boundaries of  $\alpha$  and  $\gamma$  setpoints and visualize the trend of the phase levels on time. All images and trends updates automatically when a change in the settler has occurred.

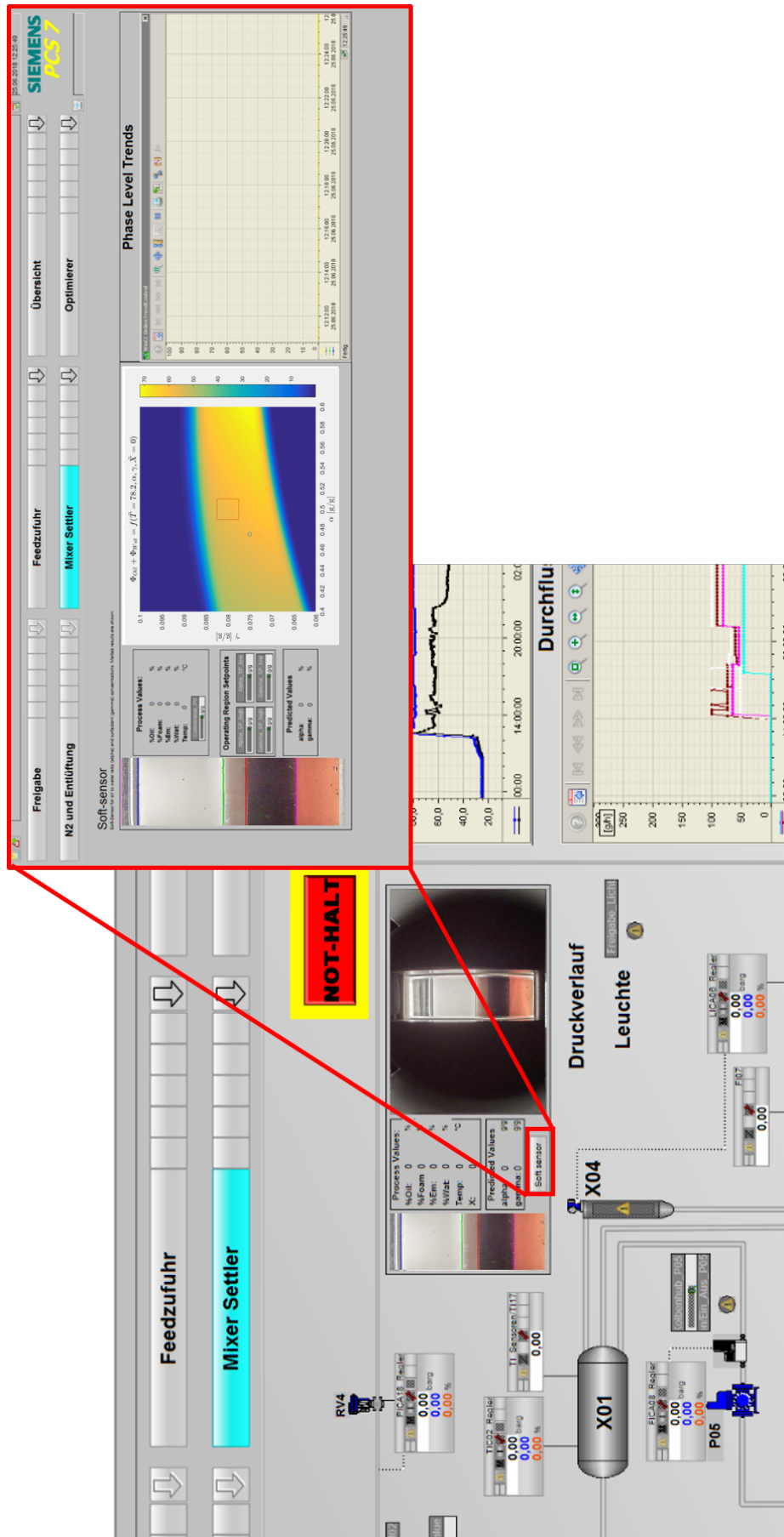


Figure 5.6: Soft-sensor and processed image integrated to the Control system PCS7

# Chapter 6

## Conclusions and Outlook

The aim of this contribution was to propose an automatic method for the quantification of the surfactant concentration and oil to water ratio, based on the evaluation of the phase separation state of microemulsions.

A suitable static model for the three phase separation behavior in microemulsions was developed based on empiric data. An operational window for temperature was found to ensure the stable operation of the settler in the three phase region. This model served as part of the solution for the full dynamic real time optimization framework on a novel process.

An image processing algorithm based on color segmentation was also developed to detect automatically the level of the phases in order to evaluate the state separation of the mixture. The methodology used was appropriately selected to exploit in a future all the color features of the phases, including the formation of the foam, the turbidity of the oil phase at high conversion and high temperatures and, the change of base color of the mixture that occurs when the catalyst is activated. The automatic image processing algorithm was tested achieving a successful detection in 76 % of the images, and a short time of processing of 1.5 seconds per image processed.

The integration of the model and the automatic image processing algorithm into the control system led to the design of the soft-sensor for the surfactant concentration and oil to water ratio in the system. An inclusion of the soft-sensor into the Siemens control system allows for an appropriate visualization of the current phase separation state allowing a stable operability of the plant in the three phase region.

Improvements in the model need to be achieved. Enhancing the experimental setting by controlling the internal temperature of the mixture, increasing the data set and performing repeated experiments, is needed to reduce the uncertainty of the measurements. Additionally, the development of a dynamic model is necessary to investigate the effect of a variable residence time in the product yield, in order to identify infeasible operating conditions for the mini-plant or to establish conceptual or constructional requirements for future improvements.





# Appendix A

## Density functions of the components

The liquid densities are calculated using the DIPPR105 equation:

$$\rho = \frac{A}{B^{1+(1-\frac{T}{C})^D}} \quad (\text{A.1})$$

where the parameters  $A, B, C, D$  depend on the component and  $T$  is the temperature in Kelvin.

The parameters of the density equation of every component is shown in table [A.1](#).

**Table A.1:** Minimum and maximum concentration of liquid components

Component	A	B	C	D
1-dodecene	2.28489	0.62755425	471.531506	0.8053307
Catalyst	0.05152	0.02941993	455.327676	0.0188297
Marlipal 27/40	0.11996	0.23297924	857.699899	0.31030365
Tridecanal	0.10697	0.147305	748.401552	0.19760173



# Bibliography

Anastas, Paul and Nicolas Eghbali

- 2010 “Green Chemistry: Principles and Practice”, *Chem. Soc. Rev.* 39 (1 2010), pp. 301-312, DOI: [10.1039/B918763B](https://doi.org/10.1039/B918763B), <http://dx.doi.org/10.1039/B918763B>. (Cit. on p. 1.)

Belič, Igor

- 2012 “Neural Networks and Static Modelling”, in *Recurrent Neural Networks and Soft Computing*, InTech, ISBN: 978-953-51-0409-4.

Beller, Matthias, Boy Cornils, Carl D. Frohning, and Christian W. Kohlpaintner

- 1995 “Progress in hydroformylation and carbonylation”, *Journal of Molecular Catalysis A: Chemical*, 104, 1, pp. 17-85, ISSN: 1381-1169.

Bora, Dibya, Anil Kumar Gupta, and Fayaz Khan

- 2015 “Comparing the Performance of L\*A\*B\* and HSV Color Spaces with Respect to Color Image Segmentation” (June 2015). (Cit. on p. 18.)

Cameron, I.T., K. Hangos, J. Perkins, and G. Stephanopoulos

- 2001 *Process Modelling and Model Analysis*, Elsevier Science, ISBN: 9780080514925.

Canny, John

- 1986 “A Computational Approach To Edge Detection”, *PAMI-8* (Dec. 1986), pp. 679-698. (Cit. on p. 20.)

Franke, Robert, Detlef Selent, and Armin Börner

- 2012 “Applied Hydroformylation”, *Chemical Reviews*, 112, 11, pp. 5675-5732, ISSN: 0009-2665.

Griffith, A. K. and N. K. Nichols

- 2000 “Adjoint Methods in Data Assimilation for Estimating Model Error”, *Flow, Turbulence and Combustion*, 65, 3, pp. 469-488, ISSN: 1573-1987.

Gujarati, D.N. and D.C. Porter

- 2009 *Basic Econometrics*, McGraw-Hill Irwin, ISBN: 9780071276252. (Cit. on p. 44.)

Hamerla, Tobias, Anke Rost, Yasemin Kasaka, and Reinhard Schomäcker

- 2013 “Hydroformylation of 1-Dodecene with Water-Soluble Rhodium Catalysts with Bidentate Ligands in Multiphase Systems”, *ChemCatChem*, 5, 7, pp. 1854-1862, ISSN: 18673880.

- Haumann, Marco, Herbert Koch, Peter Hugo, and Reinhard Schomäcker  
2002 “Hydroformylation of 1-dodecene using Rh-TPPTS in a microemulsion”, *Applied Catalysis A: General*, 225, 1, pp. 239-249, ISSN: 0926-860X. (Cit. on p. 1.)
- Ibraheem, Noor A., Mokhtar M. Hasan, Rafiqul Z. Khan, and Pramod K. Mishra  
2012 “Understanding Color Models: A review”, *ARPN Journal of Science and Technology*, 2. (Cit. on p. 18.)
- Illner, Markus  
2014 *Entwicklung einer modellbasierten Optimierungsplattform zur Online-Optimierung der Prozessführung eines Hydroformylierungsprozesses*, MA thesis, Technische Universität Berlin, Germany. (Cit. on p. 11.)
- Illner, Markus, David Müller, Erik Esche, Tobias Pogrzeba, Marcel Schmidt, Reinhard Schomäcker, Günter Wozny, and Jens-Uwe Repke  
2016a “Hydroformylation in Microemulsions: Proof of Concept in a Mini-plant”, *Industrial & Engineering Chemistry Research*, 55, 31, pp. 8616-8626, ISSN: 0888-5885 1520-5045. (Cit. on pp. 6, 8-10.)
- Illner, Markus, Tobias Pogrzeba, Marcel Schmidt, David Müller, Erik Esche, Reinhard Schomäcker, Jens-Uwe Repke, and Günter Wozny  
2016b “Hydroformylation of 1-dodecene in Microemulsions: Operation and Validation of Lab Results in a Mini-Plant”, in (Cit. on pp. 2, 10.)
- Illner, Markus, Marcel Schmidt, Tobias Pogrzeba, Carolina Urban, Erik Esche, Reinhard Schomäcker, and Jens-Uwe Repke  
2018 “Palladium-Catalyzed Methoxycarbonylation of 1-Dodecene in a Two-Phase System: The Path toward a Continuous Process”, *Industrial & Engineering Chemistry Research* (June 2018), ISSN: 0888-5885, DOI: [10.1021/acs.iecr.8b01537](https://doi.org/10.1021/acs.iecr.8b01537), <https://doi.org/10.1021/acs.iecr.8b01537>.
- Isermann, Rolf and Marco Münchhof  
2011 *Identification of Dynamic Systems: An Introduction with Applications*, Springer Berlin Heidelberg, Berlin, Heidelberg, pp. 203-221, ISBN: 978-3-540-78879-9, DOI: [10.1007/978-3-540-78879-9\\_8](https://doi.org/10.1007/978-3-540-78879-9_8).
- James, Gareth, Daniela Witten, Trevor Hastie, and Robert Tibshirani  
2014 *An Introduction to Statistical Learning: with Applications in R*, Springer Publishing Company, Incorporated, p. 430, ISBN: 1461471370, 9781461471370. (Cit. on p. 46.)
- Jürgen, Kohlpaintner Christian, Schulte Markus, Falbe Jürgen, Lappe Peter, and Weber  
2008 “Aldehydes, Aliphatic”, in *Ullmann’s Encyclopedia of Industrial Chemistry*, American Cancer Society, DOI: [doi:10.1002/14356007.a01\\_321.pub2](https://doi.org/10.1002/14356007.a01_321.pub2). (Cit. on p. 1.)

- Kahlweit, M., R. Strey, P. Firman, D. Haase, J. Jen, and R. Schomaecker  
1988 “General patterns of the phase behavior of mixtures of water, nonpolar solvents, amphiphiles, and electrolytes. 1”, *Langmuir*, 4, 3, pp. 499-511, ISSN: 0743-7463, DOI: [10.1021/1a00081a002](https://doi.org/10.1021/1a00081a002). (Cit. on p. 7.)
- Kohlpaintner, Christian W., Richard W. Fischer, and Boy Cornils  
2001 “Aqueous biphasic catalysis: Ruhrchemie/Rhône-Poulenc oxo process”, *Applied Catalysis A: General*, 221, 1, pp. 219-225, ISSN: 0926-860X, DOI: [https://doi.org/10.1016/S0926-860X\(01\)00791-8](https://doi.org/10.1016/S0926-860X(01)00791-8). (Cit. on p. 1.)
- Ljung, L.  
n.d. “Black-box models from input-output measurements”, in *IMTC 2001. Proceedings of the 18th IEEE Instrumentation and Measurement Technology Conference. Rediscovering Measurement in the Age of Informatics (Cat. No.01CH 37188)*, vol. 1, 138-146 vol.1, ISBN: 1091-5281.  
1999 *System identification (2nd ed.): Theory for the user*, Prentice Hall PTR, p. 609, ISBN: 0-13-656695-2.
- Madhav, S. and D. Gupta  
2011 “A Review on Microemulsion Based System”, *IJPSR*, 2, pp. 1888-1899. (Cit. on p. 6.)
- Meyer, K., J. P. Ruiken, M. Illner, A. Paul, D. Müller, E. Esche, G. Wozny, and M. Maiwald  
2017 “Process spectroscopy in microemulsions—setup and multi-spectral approach for reaction monitoring of a homogeneous hydroformylation process”, *Measurement Science and Technology*, 28, 3, ISSN: 0957-0233 1361-6501.
- Moeslund, T.B.  
2012 *Introduction to Video and Image Processing: Building Real Systems and Applications*, Springer London, ISBN: 9781447125037. (Cit. on pp. 17-19.)
- Müller, David  
2015 *Development of Operation Trajectories Under Uncertainty for a Hydroformylation Mini-plant*, PhD thesis, Technische Universität Berlin, Germany. (Cit. on p. 11.)
- Müller, David, Erik Esche, Diana C. López C, and Günter Wozny  
2014 “An algorithm for the identification and estimation of relevant parameters for optimization under uncertainty”, *Computers & Chemical Engineering*, 71, pp. 94-103, ISSN: 00981354.

- Müller, David, Erik Esche, Tobias Pogrzeba, Markus Illner, Felix Leube, Reinhard Schomäcker, and Günter Wozny  
2015 “Systematic Phase Separation Analysis of Surfactant-Containing Systems for Multiphase Settler Design”, *Industrial & Engineering Chemistry Research*, 54, 12, pp. 3205-3217, ISSN: 0888-5885, DOI: [10.1021/ie5049059](https://doi.org/10.1021/ie5049059). (Cit. on p. 7.)
- Müller, David, Markus Illner, Erik Esche, Tobias Pogrzeba, Marcel Schmidt, Reinhard Schomäcker, Lorenz T. Biegler, Günter Wozny, and Jens-Uwe Repke  
2017 “Dynamic real-time optimization under uncertainty of a hydroformylation mini-plant”, *Computers & Chemical Engineering*, 106, pp. 836-848, ISSN: 00981354. (Cit. on pp. 8, 10, 12.)
- Paris, Sylvain, Pierre Kornprobst, Jack Tumblin, and Frédo Durand  
2009 “Bilateral Filtering: Theory and Applications”, *Foundations and Trends® in Computer Graphics and Vision*, 4, 1, pp. 1-73, ISSN: 1572-2740, DOI: [10.1561/0600000020](https://doi.org/10.1561/0600000020). (Cit. on pp. 18, 19.)
- Peters, Catherine  
2001 *Statistics for Analysis of Experimental Data*.
- Pogrzeba, Tobias, David Müller, Tobias Hamerla, Erik Esche, Niklas Paul, Günter Wozny, and Reinhard Schomäcker  
2015 “Rhodium-Catalyzed Hydroformylation of Long-Chain Olefins in Aqueous Multiphase Systems in a Continuously Operated Miniplant”, 54 (Nov. 2015).
- Roelen, O.  
1944 “German Patent DE 849548, 1938/1952, U.S. Patent 2327066, 1943”, *Chemische Verwertungsgesellschaft Oberhausen m.b.H.* (Cit. on p. 1.)
- Ruiken, Jan-Paul  
2015 *Entwicklung der Prozessanalytik für eine Hydroformylierungsanlage: Raman-Spektroskopie von mehrphasigen Gemischen*, MA thesis, Technische Universität Berlin, Germany.
- Shlens, Jonathon  
2014 *A Tutorial on Principal Component Analysis*, vol. 51.
- Sinha, Priyanka  
2013 “Multivariate Polynomial Regression in Data Mining: Methodology, Problems and Solutions”, 4. (Cit. on p. 44.)
- Soderstrom, T.S. and P.G. Stoica  
1989 *System Identification*, Prentice Hall. (Cit. on pp. 29, 30.)
- Stubenrauch, C.  
2008 *Microemulsions: Background, New Concepts, Applications, Perspectives*, Wiley, ISBN: 9781405167826, <https://books.google.it/books?id=BeXLAAAACAAJ>. (Cit. on p. 6.)

Trefethen, L.N. and D. Bau

1997 *Numerical Linear Algebra*, Society for Industrial and Applied Mathematics, ISBN: 9780898713619.

Ünveren, H.H.Y.

2004 *Hydroformylation of Long Chain Olefins in Microemulsion*, <https://books.google.it/books?id=Q1YmtwAACAAJ>. (Cit. on p. 1.)

Van Leeuwen, P.W.N.M. and C. Claver

2006 *Rhodium Catalyzed Hydroformylation*, Springer Netherlands, ISBN: 9780306469473, <https://books.google.de/books?id=Q48MBwAAQB> AJ.

Wang, X., R. Hänsch, L. Ma, and O. Hellwich

2014 “Comparison of different color spaces for image segmentation using graph-cut”, in *2014 International Conference on Computer Vision Theory and Applications (VISAPP)*, vol. 1, pp. 301-308.

Y. Zheng, Y., J. I. Rao, and L. Wu

2010 “Edge detection methods in digital image processing”, in *2010 5th International Conference on Computer Science Education*, pp. 471-473. (Cit. on p. 19.)